Identification of a pH-Sensitive Switch in VSV-G and a Crystal Structure of the G Pre-fusion State Highlight the VSV-G Structural Transition Pathway

Frauke Beilstein, Abbas Abou Hamdan, Hélène Raux, Laura Belot, Malika Ouldali, Aurélie Albertini, Yves Gaudin

Cell Reports

Article

Identification of a pH-Sensitive Switch in VSV-G and a Crystal Structure of the G Pre-fusion State Highlight the VSV-G Structural Transition Pathway

Graphical Abstract

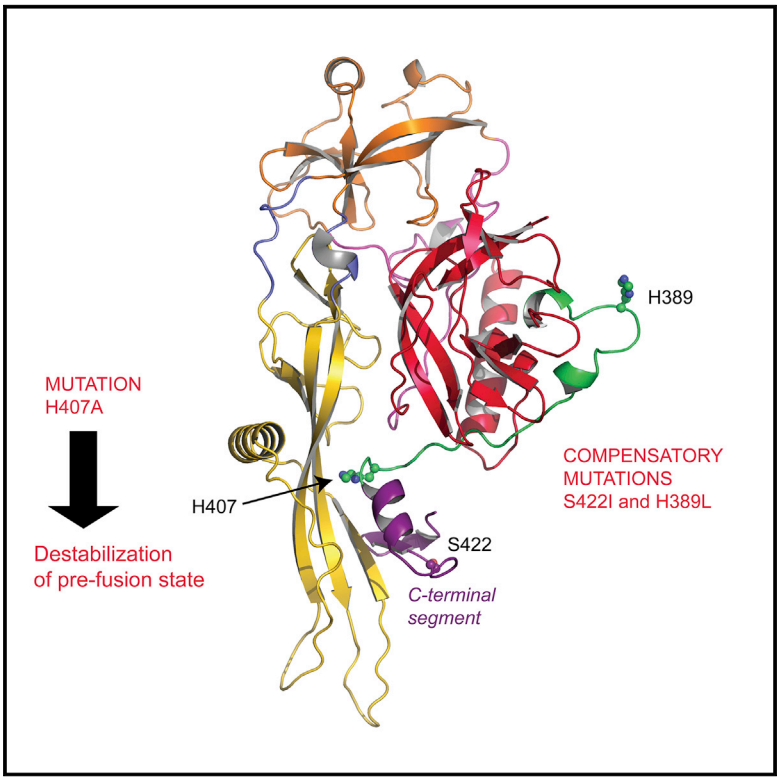

Highlights

- A VSV-G pre-fusion crystal structure reveals its C-terminal part organization
- H407A mutation affects G fusion properties by destabilizing the G pre-fusion state
- Mutants L396I and S422I compensate H407A by stabilizing the G pre-fusion state
- G structural transition is initiated in the C-terminal part of the ectodomain

Authors

Frauke Beilstein, Abbas Abou Hamdan, Hélène Raux, Laura Belot, Malika Ouldali, Aurélie A. Albertini, Yves Gaudin

Correspondence

aurelie.albertini@i2bc.paris-saclay.fr (A.A.A.), yves.gaudin@i2bc.paris-saclay.fr (Y.G.)

In Brief

Via a systematic mutational analysis, Beilstein et al. identify histidine residues acting as pH-sensitive switches during VSV-G conformational change. Selection of compensatory mutations and a crystal structure of the G pre-fusion state indicate that the conformational transition is initiated by the refolding of the C-terminal part of the G ectodomain.

Beilstein et al., 2020, Cell Reports *32*, 108042
August 18, 2020
https://doi.org/10.1016/j.celrep.2020.108042

CellPress

Cell Reports

CellPress
OPEN ACCESS

Article

Identification of a pH-Sensitive Switch in VSV-G and a Crystal Structure of the G Pre-fusion State Highlight the VSV-G Structural Transition Pathway

Frauke Beilstein,[1,2] Abbas Abou Hamdan,[1,2] Hélène Raux,[1,2] Laura Belot,[1] Malika Ouldali,[1] Aurélie A. Albertini,[1,*] and Yves Gaudin[1,3,*]

[1]Université Paris-Saclay, CEA, CNRS, Institute for Integrative Biology of the Cell (I2BC), 91198 Gif-sur-Yvette, France
[2]These authors contributed equally
[3]Lead Contact
*Correspondence: aurelie.albertini@i2bc.paris-saclay.fr (A.A.A.), yves.gaudin@i2bc.paris-saclay.fr (Y.G.)
https://doi.org/10.1016/j.celrep.2020.108042

SUMMARY

VSV fusion machinery, like that of many other enveloped viruses, is triggered at low pH in endosomes after virion endocytosis. It was suggested that some histidines could play the role of pH-sensitive switches. By mutating histidine residues H22, H60, H132, H162, H389, H397, H407, and H409, we demonstrate that residues H389 and D280, facing each other in the six-helix bundle of the post-fusion state, and more prominently H407, located at the interface between the C-terminal part of the ectodomain and the fusion domain, are crucial for fusion. Passages of recombinant viruses bearing mutant G resulted in the selection of compensatory mutations. Thus, the H407A mutation in G resulted in two independent compensatory mutants, L396I and S422I. Together with a crystal structure of G, presented here, which extends our knowledge of G pre-fusion structure, this indicates that the conformational transition is initiated by refolding of the C-terminal part of the G ectodomain.

INTRODUCTION

Vesicular stomatitis virus (VSV) is the prototype of the *Vesiculovirus* genus in the *Rhabdoviridae* family. It is an enveloped bullet-shaped virus that is responsible for epizootic outbreaks in cattle in the central and southwestern United States, Canada, and Mexico. It can also infect insects that are potential vectors of its propagation (Rozo-Lopez et al., 2018). VSV has a single transmembrane glycoprotein (G) that plays two distinct roles during viral entry (Albertini et al., 2012b). First, it mediates attachment to specific receptors that are members of the low-density lipoprotein receptor (LDL-R) family (Finkelshtein et al., 2013; Nikolic et al., 2018). Second, after virion endocytosis, it mediates fusion between viral and endosomal membranes (Albertini et al., 2012b). Fusion is triggered by endosomal acidification, which induces a conformational change of G from its pre-fusion state toward its post-fusion state. The conformational change results in the repositioning of G hydrophobic fusion loops, which are transiently able to interact with the target membrane, resulting in its destabilization and subsequently its fusion with the viral envelope. A particularity of VSV-G, which is shared with other rhabdovirus Gs, is that the low pH-induced conformational change is reversible (Doms et al., 1987; Gaudin, 2000; Gaudin et al., 1993; Kim et al., 2017) because of a pH-dependent equilibrium between the pre-fusion state and the post-fusion state, as well as intermediate conformations on the pathway of the structural transition (Albertini et al., 2012a; Gaudin, 2000; Roche and Gaudin, 2002; Zagouras and Rose, 1993).

VSV-G is the only class III fusion protein for which the trimeric structures of both pre-fusion and post-fusion states of the ectodomain have been determined (Baquero et al., 2015; Roche et al., 2006, 2007). The polypeptide chain of the G ectodomain folds into three distinct domains (Baquero et al., 2015). The fusion domain (FD) consists of an extended β sheet structure at the tip of which are located the two fusion loops that constitute the membrane-interacting motif of the G ectodomain (Roche et al., 2006; Stanifer et al., 2011; Sun et al., 2008). FD is inserted in a loop of a pleckstrin homology domain (PHD) that is itself inserted into a central trimerization domain (TrD) involved in the trimerization of the molecule in both pre-fusion and post-fusion states. These rigid domains are connected by segments (R1 to R5), which undergo major refolding events during the structural change (Baquero et al., 2015; Roche et al., 2007). In the post-fusion state, the core of the trimer is a six-helix bundle, which is similar to that found in the post-fusion state of class I proteins (Harrison, 2015; Roche et al., 2006).

All data obtained so far indicate that the pathway of the structural transition involves monomeric intermediates (Albertini et al., 2012a; Baquero et al., 2017; Doms et al., 1987). A crystalline form of the Chandipura virus (CHAV, another vesiculovirus) G ectodomain has been obtained whose asymmetric unit contains two conformations that are both distinct from the pre-fusion

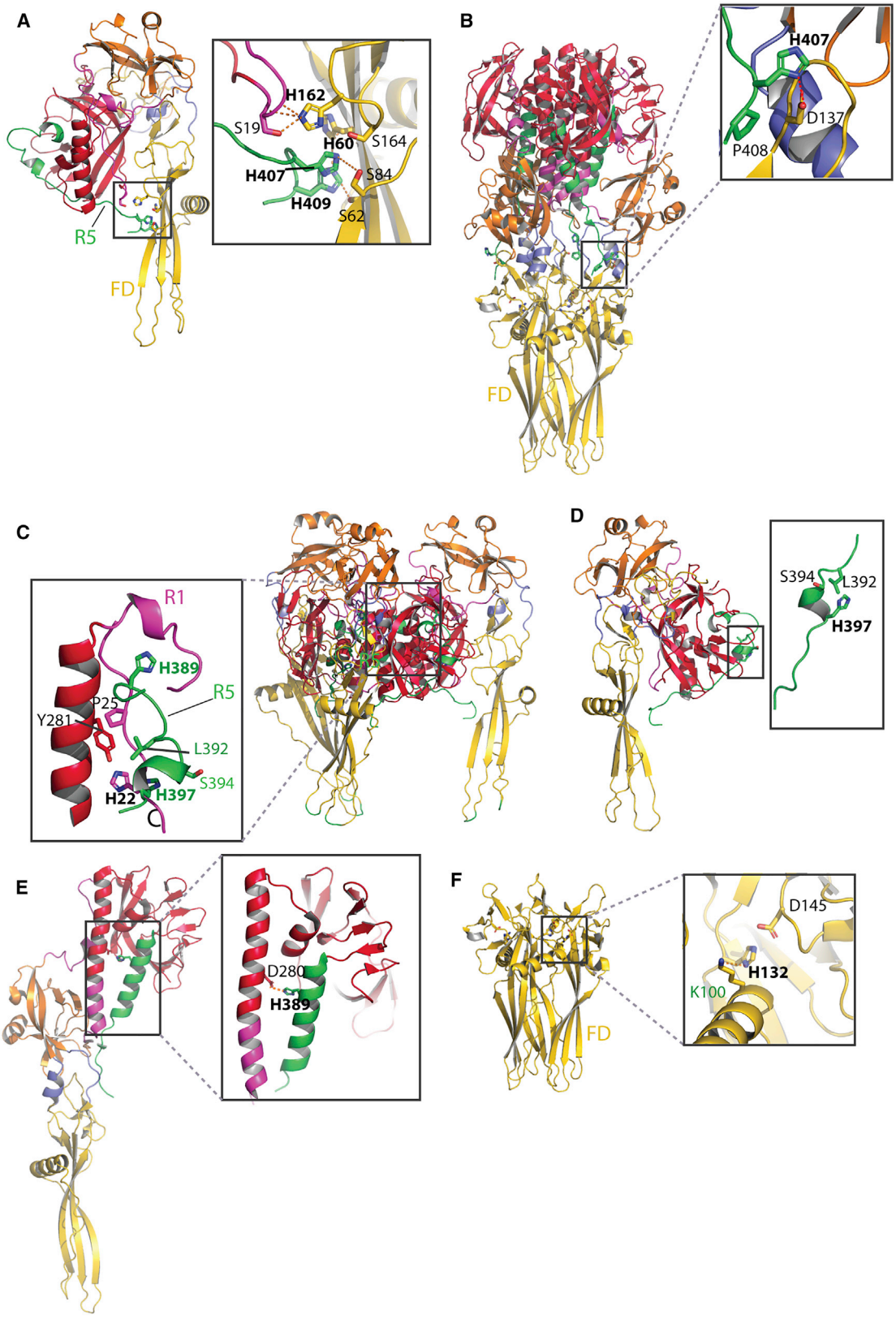

(legend on next page)

and post-fusion protomer structures (Baquero et al., 2017). The first conformation, which was considered an early intermediate (EI), resembles the VSV-G pre-fusion protomer with one major difference: the R5 segment has already left the hydrophobic grooves it occupies in the pre-fusion conformation. The second conformation of CHAV-G in this crystal corresponds to a late intermediate (LI). It resembles the post-fusion protomer, although the refolding of segments R1, R4, and R5 is still incomplete. These two structures offer a plausible pathway for the conformational change, which begins R5 leaving the TrD groove it occupies in the pre-fusion conformation (Baquero et al., 2017). This pathway is also in agreement with two recent crystal structures of monomeric rabies virus (RABV) G that are similar to the VSV EI and LI conformations (Yang et al., 2020). This is in contrast with the proposed model, largely based on the analogy with class I fusion glycoproteins. In this model, the conformational change is initiated by refolding of segments R2 and R3 and followed by the elongation of the central helix because of R4 refolding, leading to the formation of an elongated structure with the transmembrane domain located at one tip and the fusion loops at the other and thus bridging the viral and cellular membranes (Harrison, 2015; Roche et al., 2007).

We previously demonstrated that acidic residues in the six-helix bundle of the post-fusion conformation play the role of pH-sensitive molecular switches that trigger the reverse structural transition of VSV-G from the post-fusion toward the pre-fusion state (Ferlin et al., 2014). However, residues playing the role of switches triggering the low pH-induced conformation (i.e., from the pre-fusion toward the post-fusion conformation) have not been identified. As in other pH-sensing proteins (Charafeddine et al., 2019; Fritz et al., 2008; Srivastava et al., 2007; Vercoulen et al., 2017; Williamson et al., 2015; Wu et al., 2019), histidines have been discussed as playing a key role, because their side chain pKa (negative base-10 logarithm of the acid dissociation constant) is slightly above 6 (Carneiro et al., 2003; Roche et al., 2007). Indeed, a cluster of four histidine residues (in positions 60, 162, 407, and 409) in the pre-fusion structure has been proposed to have such a role as a pH-sensitive switch (Figure 1A; Roche et al., 2007).

In this work, we have mutated eight conserved histidine residues (H22, H60, H132, H162, H389, H397, H407, and H409) into alanine. Mutants H389A and H407A were affected in their fusion properties. Because aspartic acid in position 280 is facing the histidine in position 389, we also constructed mutant D280L, which also appeared to have reduced fusion activity. The ability of those mutants to adopt the pre-fusion conformation was also investigated using the CR3 domain of the LDL-R as a conformational probe. This revealed that for mutant H407A, the equilibrium between the states is shifted toward G conformations that are unable to recognize CR3.

Mutants H389A, H407A, and D280L were introduced in the genome of recombinant VSV. Mutant H389A could be obtained without selection of compensatory mutations. In contrast, a single passage of recombinant viruses D280L and H407A resulted in pseudorevertants with a second mutation.

Previous VSV-G structures were obtained with a soluble ectodomain generated by limited proteolysis with thermolysin (G_{th}, amino acid residues 1 to 422) and only revealed the structure of the first 413 residues of G in the pre-fusion conformation and the first 410 residues of G in the post-fusion conformation (Roche et al., 2006, 2007). Here, we expressed an ectodomain of G encompassing residues 1 to 440 ($G_{1–440}$) in *Drosophila* S2 cells. $G_{1–440}$ has been crystallized in its pre-fusion conformation, revealing the structural organization of residues 414 to 432 and shedding light on the role of the compensatory mutation.

Globally, besides extending our knowledge about the VSV-G pre-fusion structure, this work demonstrates that H407 plays a key role in the structural transition. Furthermore, the pre-fusion structure and locations of H407A compensatory mutations are in agreement with a conformational change initiated by the movement of the C-terminal segment R5.

RESULTS

Mutant Construction, Expression, and Transport

The G ectodomain contains 14 histidines (Table S1). Two of them, H8 and H80, have already been characterized. H8 slightly contributes to CR domain recognition (Nikolic et al., 2018). A mutation of conserved H80 into an alanine or a glutamate abolishes G fusion properties (Baquero et al., 2017). Four of the histidines (H33, H133, H168, and H226) are solvent exposed and not conserved. The environment of the other eight histidines changes during the structural transition of the molecule from pre-fusion to post-fusion (Figure 1). Among those eight histidines, H60 and H162 (located in FD), together with H407 and H409 (located in R5), constitute a cluster that locks the pre-fusion protomer (Figure 1A). It has been proposed that their protonation might create a repulsive force between FD and the C-terminal part of the molecule, thus initiating G conformational change (Baquero et al., 2017; Roche et al., 2007). Furthermore, residue H407, which is part of the conserved dipeptide H407-P408, has been suggested to stabilize the post-fusion protomer by making a salt bridge with D137 (Figure 1B; Roche et al., 2006). H22 (R1) and H397 (R5) are located at the trimeric interface of the

Figure 1. Location of Histidine Residues Mutated in This Study in the 3D Structure of G

(A) Pre-fusion protomer of G and close up of the environment of the histidine cluster H60, H162, H407, and H409.

(B) Post-fusion trimer and close up of the environment of H407 in a protomer.

(C) Pre-fusion trimer and close up of the environment of H22, H389, and H397 at the trimeric interface. Residues belonging to different chains are labeled in different colors (black and green).

(D) Pre-fusion monomer and close up of the environment of H397.

(E) Post-fusion protomer of G and close up of H389 and D280.

(F) Post-fusion trimer and close up of the environment of H132. Residues belonging to different chains are labeled in different colors (black and green).

TrD is in red, PHD is in orange, FD is in yellow, segments R1 and R4 are in pink, segments R2 and R3 are in blue, and the C-terminal segment (R5) is in green. Histidines that have been mutated in this work are in bold.

pre-fusion state (Figures 1C and 1D; Roche et al., 2007). This is also the case for H389 (R5), which forms a salt bridge with the lateral chain of residue D280 in the six-helix bundle of the post-fusion state (Figures 1C and 1E; Roche et al., 2006). Finally, the side chain of residue H132 makes a hydrogen bond with the C = O group of K100 in the post-fusion conformation (Figure 1F; Roche et al., 2006).

We decided to replace these eight histidines and constructed mutants H22A, H60A, H132A, H162A, H389A, H397A, H407A, and H409A. We also constructed the mutant D280L.

BSR (clones of BHK-21) and HEK293T cells were transfected with pCAGGS plasmids, allowing the expression of wild type (WT) and mutant G. Protein expression and cell surface localization of mutant G proteins were analyzed by indirect immunofluorescence (IF) microscopy using monoclonal antibody (mAb) 8G5F11, directed against the G ectodomain, on both permeabilized and non-permeabilized BSR cells (Figure 2A). mAb 8G5F11 targets a conformational epitope located in the amino-terminal part of the helix that extends from residue 241 to residue 249 and is located at the top of PHD in the pre-fusion conformation (Munis et al., 2018). In BSR cells, all mutant Gs, except H132A, were transported to the cell surface, indicating that they can leave the endoplasmic reticulum (ER) and thus have the characteristics of folded proteins. IF after cell permeabilization revealed that H132A appears to accumulate in the ER, suggesting that this mutant cannot fold properly.

G expression in HEK293T cells and the amount of G protein present on their surface was also quantified using flow cytometry (Figures 2B and 2C). This confirmed that H132A was not folded properly: it was detected at the surface of only ~28% of the cells, and when detected, its average concentration at the surface of the cell was only 9% of that of WT. For all other mutants, the percentage of cells expressing G at their surface ranges from 80% (for H407A) to virtually 100%. Globally, the average concentration of mutant Gs at the viral surface was similar to WT (ranging from 86% to 101%) except for mutant H407A, for which it was only ~25% of WT (Figures 2B and 2C).

Fusion Properties of G Mutants

The fusion activity was assayed using a previously described cell-cell fusion assay (Baquero et al., 2017; Ferlin et al., 2014). BSR cells were co-transfected with a plasmid encoding the RABV phosphoprotein fused with the green fluorescent protein (P-GFP) and the plasmid encoding WT or mutant Gs. Then 24 h after transfection, the cells were exposed for 10 min (at 37°C) to DMEM adjusted to the required pH, which was then replaced by DMEM buffered at pH 7.4. The cells were then kept at 37°C for 1 h before fixation. P-GFP allows easy detection of the transfected cells and, because it is unable to diffuse passively in the nucleus (Pasdeloup et al., 2005), counting of nuclei per syncytia.

Mutants H22A, H60A, H162A, H397A, and H409A exhibited fusion activity similar to that of the WT virus with similar pH dependence (i.e., massive syncytia formation at pH 6 and below and residual fusion activity at pH 6.5 and above). Mutants H389A and D280L had reduced fusion activity: for mutant H389A, massive syncytia were only detected at pH 5.5 or below, and for mutant D280L, only small syncytia were detected below pH 5.5. Finally, mutant H407A had no fusion activity (Figure 3). The low level of cell surface expression of mutant H407A (Figures 2B and 2C) may partly explain this absence of fusion activity. To overcome the difference in cell surface expression level, we transfected BSR cells with a quarter of the amount of the plasmid expressing WT G and twice the amount of the plasmid expressing mutant H407A. The pH dependence of syncytia formation was unchanged for WT G; however, small syncytia were observed at pH 5 (but not at pH 5.5) for mutant H407A, demonstrating residual fusion activity for this mutant (Figure S1).

LDL-R CR3 Domain Recognition by G Mutants

We have recently demonstrated that the CR2 and CR3 domains of the LDL-R receptor bind VSV-G only at high pH when G is in its pre-fusion conformation (Nikolic et al., 2018). We used the CR3 domain as a conformational probe and investigated the binding of glutathione S-transferase (GST)-CR3 (in which CR3 is C-terminally fused to the GST protein) to VSV-G. For this, 24 h post-transfection, HEK293T cells were incubated with mAb 8G5F11. Then, green fluorescent anti-immunoglobulin G (IgG) secondary antibodies and GST-CR proteins fluorescently labeled with ATTO550 were simultaneously added (Figures 4A and 4B).

Most mutants bind GST-CR3 as efficiently as WT G (~90% to 95% of cells expressing G were positive for CR3 binding). The exceptions were mutants H409A and D280L, which were slightly but significantly affected in their ability to bind CR3, and H407A, for which only ~13% of the cells expressing G were positive for CR3 binding. However, CR3 recognition by mutant H407A was significantly higher than recognition by mutant R354Q that is mutated in the G CR binding domain (Nikolic et al., 2018) and included as a negative control (Figures 4A and 4B). Because Residue H407 is far from the CR binding domain of G (Nikolic et al., 2018), this suggests that for this mutant, the equilibrium between the states is shifted toward G conformations that are unable to recognize CR3.

Oligomerization Status and Post-fusion Conformation of Mutant H407A

The H407A mutation has the strongest impact on G behavior. Because residue H407 is also involved in the stabilization of the post-fusion conformation, we analyzed the effect of H407A mutation on the stability of the post-fusion state. For this, we took advantage of the G pre-fusion trimer that, although detected at the viral surface (Libersou et al., 2010), is not stable in solution: only monomers are detected at high pH (Albertini et al., 2012a; Doms et al., 1987), whereas at low pH, the G post-fusion trimer is stable. Monomers and post-fusion trimers can be separated in the sucrose gradient (Doms et al., 1987; Ferlin et al., 2014): monomeric G is recovered in the upper fractions 10 and 11, whereas trimeric G is found between fraction 7 and fraction 9 (Figure 4C).

We analyzed the oligomeric status of WT G and mutant H407A after detergent solubilization (Figure 4C). For both WT and mutant G, only monomers were detected above pH 7 and trimers were observed at pH 6.5 and 6. This suggests that H407A mutation probably does not affect post-fusion-state stability.

We also investigated the structure of full-length mutant H407A at the surface of pseudotyped VSVΔG-GFP, a recombinant VSV

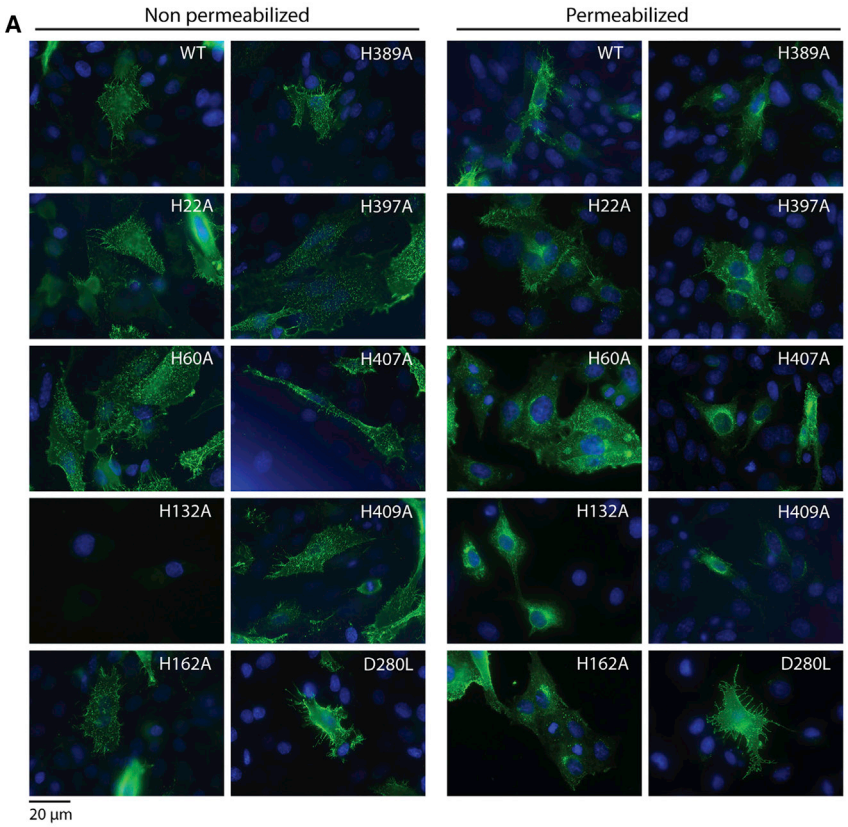

Figure 2. Expression and Transport of Mutated G in BSR and HEK293T Cells

(A) Expression and subcellular localization of G proteins in BSR cells. Epifluorescence images of transfected cells are shown. At 24 h post-transfection, cells were permeabilized (or not) and fixed, and G was detected by immunostaining with mAb 8G5F11, which was subsequently detected using a goat anti-mouse IgG secondary antibody conjugated to Alexa Fluor 488. Nuclei were stained with DAPI.

(B) Surface expression of G in HEK293T cells. The surface G protein expression was detected with mAb 8G5F11 and a goat anti-mouse IgG secondary antibody conjugated to Alexa Fluor 488. A total of 10,000 cells were counted by flow cytometry. In each frame, the black curve corresponds to the fluorescence of untransfected cells, the blue curve corresponds to the fluorescence of cells transfected by pCAGGS plasmids encoding WT G, and the red curve corresponds to the fluorescence of cells transfected by pCAGGS plasmids encoding the indicated mutant.

(C) Quantification of surface expression of mutant G expressed in HEK293T cells. The percentage of cells expressing G is in red. The surface expression (in blue) (assimilated to the mean fluorescence intensity [MFI] of G-expressing cells) is expressed as a percentage of that of WT G. Values are the average of at least 3 independent experiments ± the standard deviation. Statistically significant differences with WT are indicated by black stars and with H132A are indicated by red ones (*$p < 0.05$, **$p < 0.005$, ***$p < 0.0005$, two-tailed Student's t test).

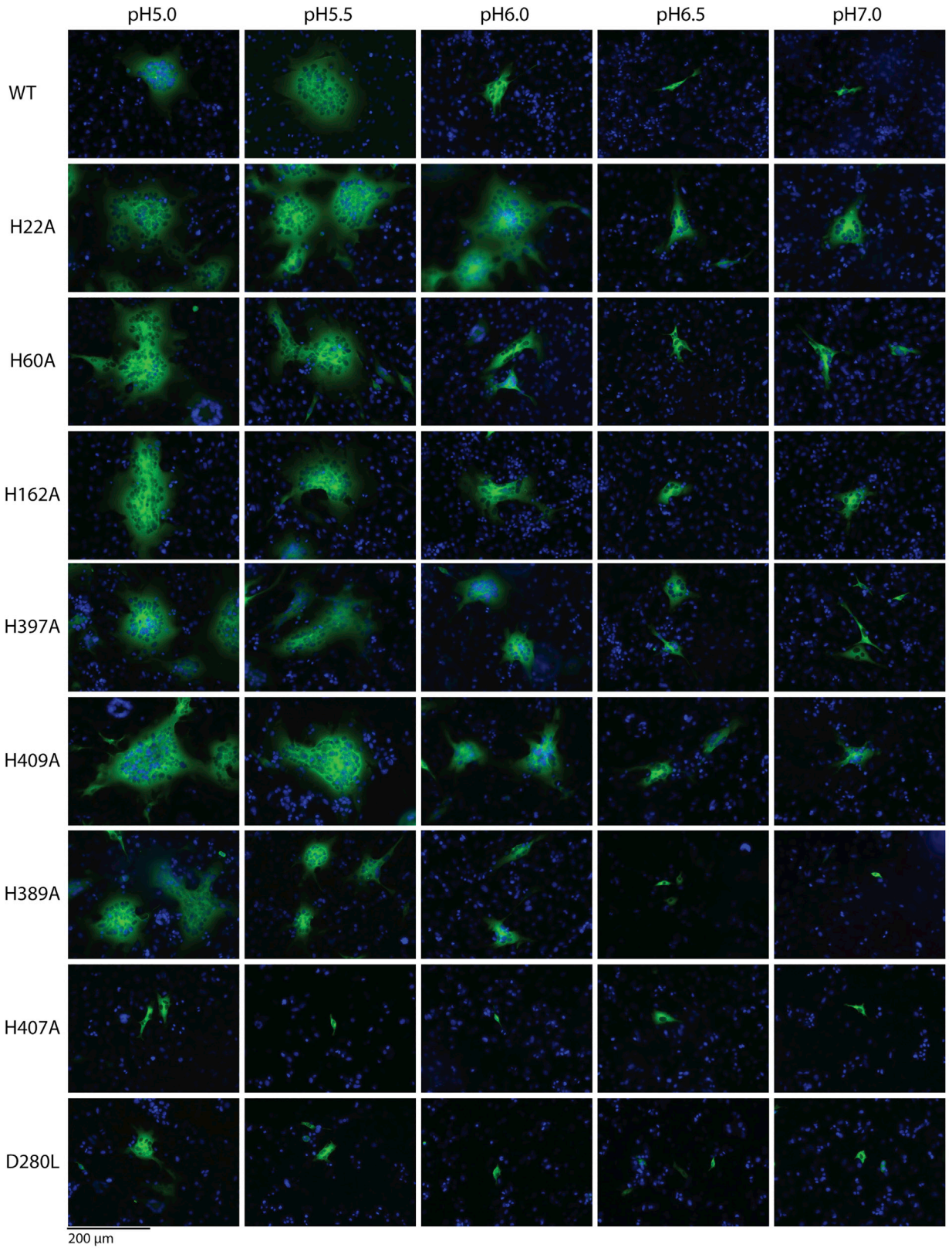

(legend on next page)

in which the G envelope gene was replaced by the GFP gene. At pH 7.5, both WT and mutant G formed the characteristic 7-nm-wide layer (Libersou et al., 2010). At pH 5.5, at the surface of the pseudotyped particles, the spikes were individualized, allowing the visualization of 12-nm-long spikes in their post-fusion conformation that stood perpendicular to the membrane (Figure 4D).

Finally, we expressed a soluble G ectodomain ($G_{1–440}$ with a C-terminal tandem StrepTag) in the *Drosophila* Schneider S2 cell line for both WT and mutant H407A G. Both WT and mutant $G_{1–440}$ were purified. For both proteins, after incubation at pH 5.5, negative-staining electron microscopy (EM) revealed the typical, 12-nm-long, post-fusion trimeric conformation. In the absence of membranes, they self-associated through their fusion loops to form rosettes made of a few trimers. In the presence of liposomes, they inserted in the membrane via their hydrophobic fusion loops (Figure 4E). Therefore, there was no major difference between WT G and mutant H407A in that both behave in the same way as G_{th} (the soluble ectodomain, comprising residues 1 to 422, generated by G_{th}) (Albertini et al., 2012a).

Altogether, these results indicate that mutant H407A can transit toward the post-fusion conformation and behaves similar to WT G at low pH.

Attempt to Generate Recombinant Viruses and Selection of Compensatory Mutations

Mutations presenting the strongest phenotype difference with WT G (i.e., D280L, H389A, and H407A) were introduced in the viral genome. We easily generated recombinant VSV expressing G bearing the H389A mutation (VSV-G.H389A). Because the other mutants (VSV-G.D280L and VSV-G.H407A) were not generated spontaneously, we employed a complementation strategy to support their growth. The recovery of the recombinant VSV was supported by the expression of functional WT VSV-G protein in *trans* from a transfected plasmid (Baquero et al., 2017; Ferlin et al., 2014; Jeetendra et al., 2003; Stanifer et al., 2011). To generate virus particles containing only the fusion-defective VSV-G expressed from the viral genome, viruses present in the supernatant were amplified in cells that lack the *trans*-complementing VSV-G plasmid.

Using this approach, we recovered infectious recombinant viruses for each mutant, from which the G gene was sequenced. In the case of VSV-G.H389A, no additional nucleotide change was detected. This was not the case for the other recombinant viruses. In the case of mutant D280L, sequence analysis revealed a single additional coding change in the genome, resulting in the compensatory replacement of H389 by a leucine (leading to the double mutant VSV-G.D280L/H389L). In the case of mutant H407A, sequence analysis of independent clones revealed two distinct compensatory mutations: the first one resulted in the replacement of L396 by an isoleucine (leading to the double mutant VSV-G.L396I/H407A), and the second one resulted in the replacement of S422 by an isoleucine (leading to the double mutant VSV-G.H407A/S422I).

Characterization of Recombinant Viruses

We compared the one-step growth curves of VSV WT and mutants VSV-G.H389A, VSV-G.D280L/H389L, VSV-G.L396I/H407A, and VSV-G.H407A/S422I in BSR cells infected at an MOI of 3. The growth curves of all mutants were slightly affected, with a titer decrease after 16 h of infection ranging from 0.5 log (VSV-G.H389A, VSV-G.D280L/H389L, and VSV-G.L396I/H407A) to 1.5 log (VSV-G.H407A/S422I) (Figure 5A).

We characterized further the properties of mutants D280L/H389L, L396I/H407A, and H407A/S422I, as well as the mutant harboring the single mutations of H389L, L396I, and S422I. BSR and HEK293T cells were transfected with pCAGGS plasmids, allowing the expression of WT and mutant G.

Indirect IF microscopy using mAb 8G5F11, on both permeabilized and non-permeabilized BSR cells, indicated that all mutant Gs were transported to the cell surface (Figure 5B). The amount of G protein present at the surface of HEK293T cells was also quantified using flow cytometry (Figures 5C and 5E). Mutant Gs were detected at the surface of more than 95% of the cells. The average concentrations of mutants H389L, D280L/H389L, L396I, and S422I at the cell surface of the cell were similar to that of WT, ranging from 88% to 119% when normalized to WT. The average concentrations were slightly lower for the other mutants, ~60% for L396I/H407A and ~50% for H407A/S422I, which were, however, significantly more present than mutant H407A at the cell surface.

We simultaneously investigated the mutant ability to bind the CR3 domain (Figures 5D and 5E). Mutants L396I and S422I bind GST-CR3 as efficiently as WT G. Mutant H389L was slightly but significantly affected. The double mutants L396I/H407A and D280L/H389L were more affected: only ~60% of the cells expressing G were positive for CR3 binding. The double mutant H407A/S422I was even more affected, with only ~30% of the cells expressing G positive for CR3 binding. However, the double mutants L396I/H407A and H407A/S422I significantly better recognized CR3 compared with the single mutant H407A.

When the fusion activity of the mutants was assayed, they all exhibited pH dependence similar to that of WT. However, whereas mutants L396I and S422I do not affect the size of the syncytia, mutant H389L and all double mutants form smaller syncytia. This was particularly obvious for mutants L396I/H407A and H407A/S422I (Figure 5F).

Finally, we investigated the morphology of the recombinant viruses and their spikes after negative staining (Figure 6). At high pH, mutants VSV-G.D280L/H389L and VSV-G.L396I/H407A behaved like VSV WT. Viral particles had the characteristic bullet shape described in previous studies and exhibited the characteristic layer of spikes of ~7 nm in width. Mutant VSV-

Figure 3. Fusion Activity of WT and VSV-G Mutants Analyzed in a Cell-Cell Fusion Assay

BSR cells were transfected with plasmids expressing VSV-G (either WT or mutant) and P-GFP, allowing easy observation of syncytia. At 24 h post-transfection, the cells were exposed for 10 min to DMEM adjusted to the indicated pH, which was then replaced by DMEM at pH 7.4. The cells were then kept at 37°C for 1 h before fixation. The mutants are presented in the figure in the order of decreasing fusion efficiency, starting with WT G. Nuclei were stained with DAPI. All images are representative examples from at least three independent experiments. See also Figure S1.

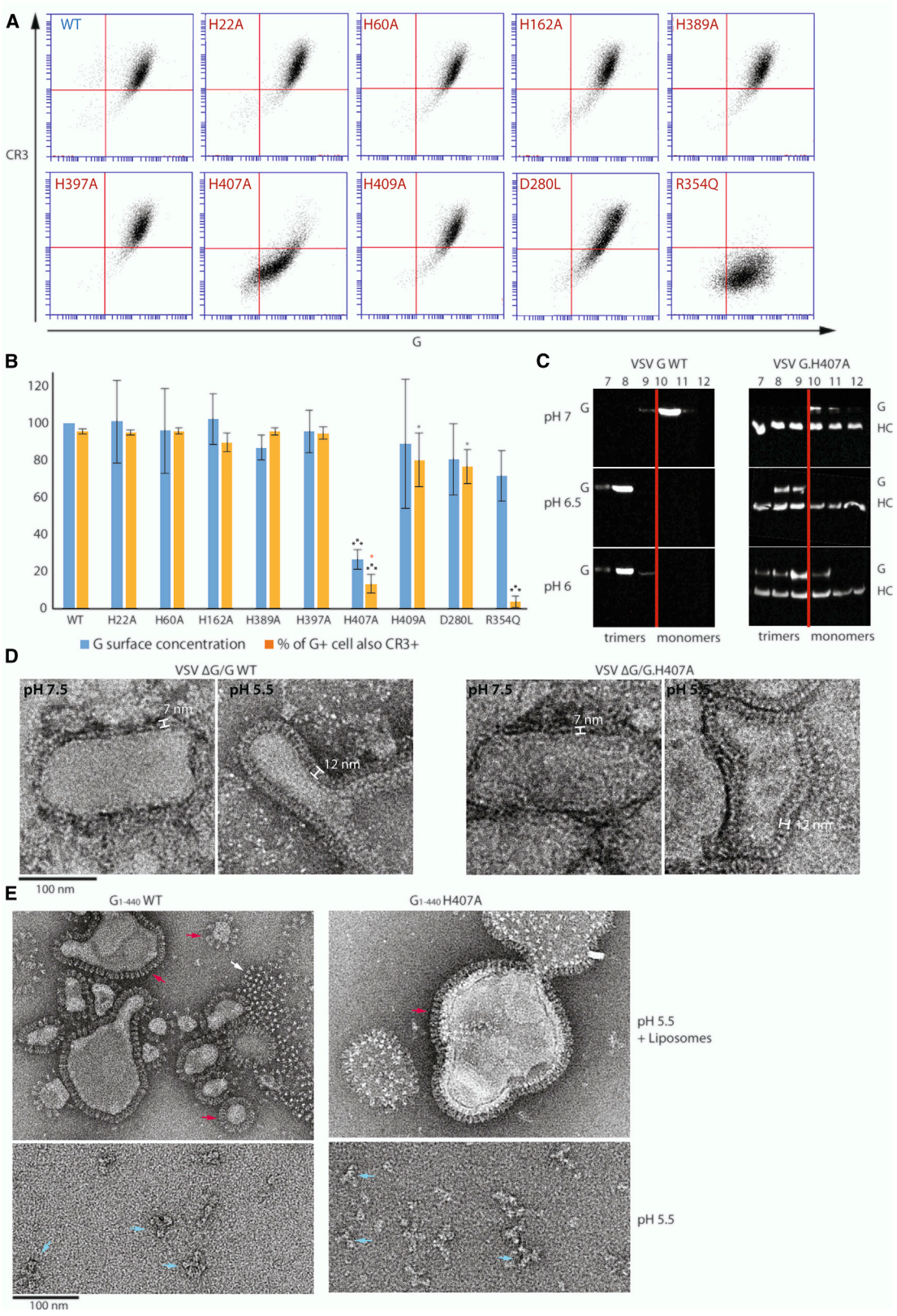

(legend on next page)

G.H407A/S422I behaved in a significantly different way. Virions were aggregated but seemingly unfused, as observed with VSV WT and RABV at intermediate pH when G is in an intermediate conformation exposing fusion loops. At pH 6, as previously described (Libersou et al., 2010), viral particles were aggregated, and virions had often lost their bullet shape and were sometimes fused. When spikes were observed at the surface of isolated virions, they exhibited the post-fusion conformation.

X-Ray Structure of the Recombinant G Ectodomain

The structure of the pre-fusion state of G_{th} was only known until residue 413, whereas that of the post-fusion state of G_{th} was only known until residue 410 (Roche et al., 2006, 2007). Therefore, the structure of the local environment of residue 422 was not known. In an attempt to get structural information on the C-terminal part of the G ectodomain, we screened several crystallization conditions for $G_{1–440}$, obtained crystals at pH 7.5, and determined the structure of a trimeric pre-fusion conformation at a 2.1 Å resolution (Figure 7A). The organization of the G protomer in the crystalline lattice (P622 space group) was similar to that of the G_{th} pre-fusion conformation. The polypeptidic chain could be traced up to residue 432. The root-mean-square deviation (RMSD, calculated for the Cα backbone) between the G_{th} pre-fusion protomer and the $G_{1–440}$ pre-fusion protomer calculated for residues 1 to 63 and 127 to 410 was 0.8 Å, indicating that these regions of G were identical in both crystals. However, FD was tilted at an angle of 11° relative to the rest of the protein (Figure 7B).

The C-terminal part of $G_{1–440}$, which is ordered in the crystal, is made of an α helix (residues 409 to 416), followed by a kinked region, and ending with a β turn between Pro 418 and Glu 421 and a short β-hairpin structure (residues 422–432). The hairpin structure interacts with strand 79–84 of the FD β sheet through hydrogen bonds between the main chains of both segments and between the lateral chains of residues H80 and E421 (Figure 7C). The structure of the C-terminal part of G is also stabilized by the insertion of the lateral chain of F109 into a hydrophobic pocket made by residues I82, A413, L417, and L423 and the $C_βH_2$ group of the lateral chain of H80. Therefore, globally, the C-terminal part is packed against FD and contributes to the locking of the G protomer in its pre-fusion state.

DISCUSSION

Many viral fusion Gs undergo a low-pH fusogenic conformational change in the endosomal environment. Histidines, because of their pKas of ~6, which match the endosomal pH, have been speculated to play an important role as acidic pH sensors. However, evidence for such a role has been obtained only for tick-borne encephalitis virus (Fritz et al., 2008) and for influenza virus (Mair et al., 2014). The systematic mutational analysis presented in this work reveals the important role of the pair of residues D280 and H389 in the stabilization of the post-fusion state and the key role of H407 in the structural transition. The X-ray structure of $G_{1–440}$, which is also presented in this work, has a higher resolution than the previous G_{th} crystalline pre-fusion structure (Roche et al., 2007) and provides views of the organization of the G ectodomain C-terminal segment that were missing in previously reported structures (Roche et al., 2006, 2007). Together with the compensatory mutations of mutant H407A, this structure sheds light on the pathway of the structural transition and reinforces the idea that it is initiated by refolding of the C-terminal part of the G ectodomain (Baquero et al., 2017).

The C-Terminal Part of G Contributes to the Locking of the Ectodomain in Its Pre-fusion State

This X-ray structure of the G ectodomain completes our understanding of the structure of the class III pre-fusion state. It reveals that in this state, the C-terminal part (from residue 407 to residue 425) largely interacts with FD of the same protomer and therefore contributes to the stabilization of the pre-fusion complex. These tight interactions may explain the tilt of FD relative to the rest of the molecule when compared with the pre-fusion structure of G_{th} (Figure 7B). They have to be broken for the molecule to initiate its structural change.

The transmembrane (TM) domain is predicted to extend from residue 449 to residue 466. The structural organization of the last 16 residues of the ectodomain is therefore still unknown. The C = O

Figure 4. Analysis of Cell Surface Expression, CR Domain Binding Properties, and the Oligomerization State of WT and Mutant G

(A) Flow cytometry analysis of the expression of WT and mutant G at the surface of HEK293T cells and of the binding of fluorescent GST-CR3. After 24 h of transfection, cell surface expression of WT and mutant G was assessed using anti-G mAb 8G5F11 directly on living cells at 4°C during 1 h. Cells were then incubated simultaneously with anti-mouse Alexa Fluor 488 and the indicated GST-$CR^{ATTO550}$. Cells transfected with a G construct that was still able to bind GST-CR proteins exhibited red fluorescence because of the ATTO550 dye.

(B) Quantification of surface expression and CR3 binding properties of mutant G expressed in HEK293T cells. The surface expression (in blue) is expressed as a percentage of that of WT G. The percentage of cells expressing G that are also positive for CR3 is in orange. Values are the average of at least 3 independent experiments (like the one presented in A) ± the standard deviation. Statistically significant differences with WT are indicated by black stars and with R354Q are indicated by red ones (*$p < 0.05$, **$p < 0.005$, ***$p < 0.0005$).

(C) Oligomerization assay of WT and mutant H407A. At 24 h after transfection, HEK293T cells were lysed, and the cellular extracts were overlaid on a 5% to 20% continuous sucrose gradient in 100 mM NaCl-0.1% Triton, adjusted to the required pH. After centrifugation for 16 h at 35,000 rpm, 12 fractions were collected from the bottom of the gradient. For WT G, 20 μL of each fraction were directly analyzed by western blot. Because of lower expression, mutant G protein was immunoprecipitated using mAb 8G5F11 before analysis by western blot with a mouse mAb directed against the C-terminal, intraviral part of G (P5D4; Sigma). G found in fractions 10 and 11 corresponds to a monomer, whereas G found in fractions 7 to 9 corresponds to the post-fusion trimer. The data presented in this figure are representative examples from three independent experiments. HC, heavy chain of 8G5F11 revealed during western blot.

(D) Negative-staining EM of VSVΔG-GFP pseudotyped either by WT or mutant H407A. At pH 7.5, both WT and mutant G formed the characteristic 7-nm-wide layer at the pseudotype surface. At pH 5.5, both pseudotypes exhibit 12-nm-long individualized spikes corresponding to the post-fusion trimer that stands perpendicular to the membrane.

(E) Negative-staining EM of purified WT and mutant H407A $G_{1–440}$. Before EM observation, the protein was incubated at pH 5.5 in the presence or absence of liposomes. Cyan arrows indicate rosettes of $G_{1–440}$ in its post-fusion conformation. Red arrows indicate Gs with the typical trimeric post-fusion state anchored in the membrane by their fusion loops. The white arrow indicates post-fusion trimers in solution tending to associate and to form a lattice via lateral contacts.

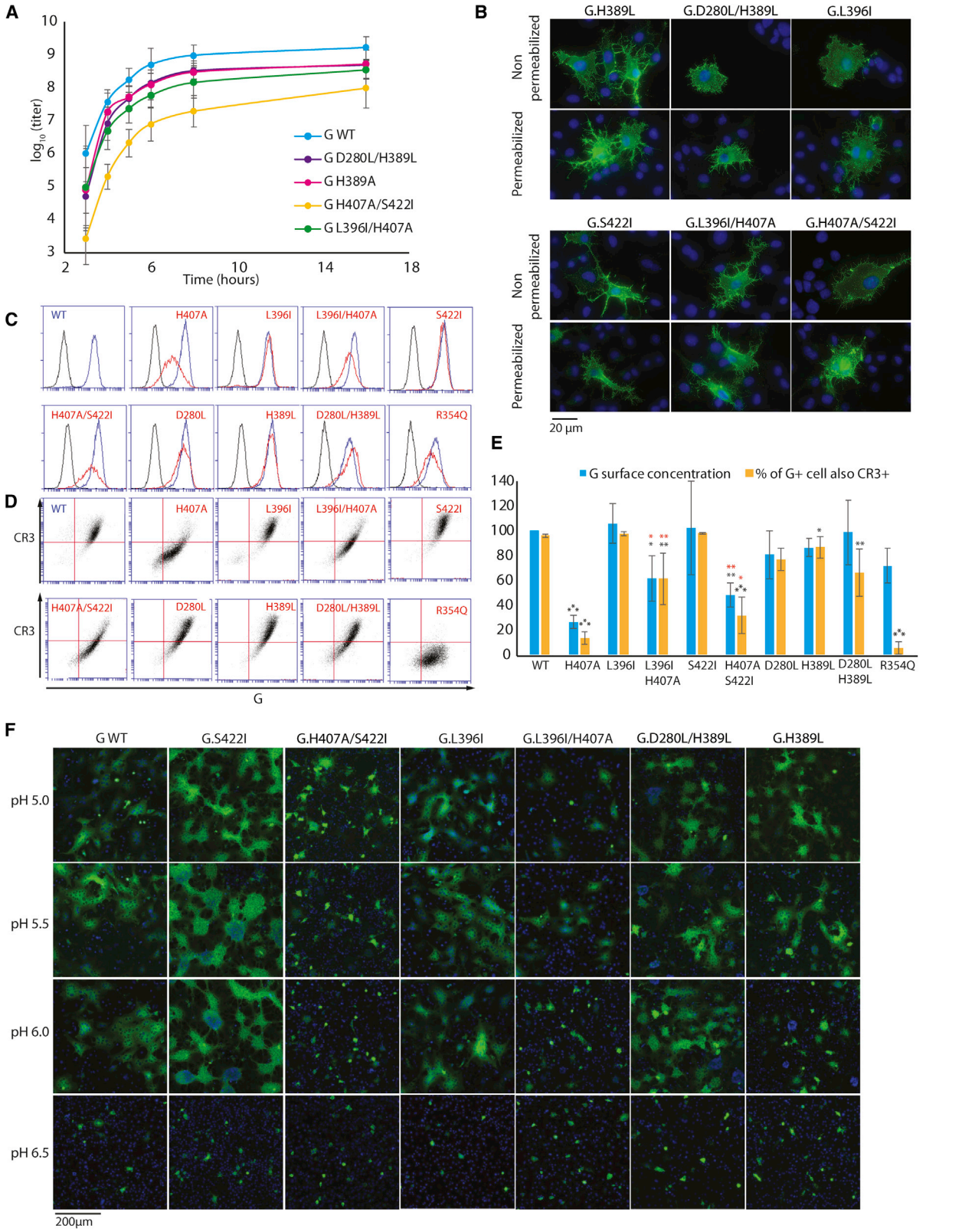

(legend on next page)

group of lysine 432 is still ~2 nm from the membrane: therefore, the way the C-terminal segment is joining the membrane should be rather direct. This explains why the deletion of the 13 membrane-proximal amino acids (433 to W445) dramatically reduced cell-cell fusion activity (Jeetendra et al., 2003). This is consistent with tomography reconstructions of the pre-fusion trimer at the viral surface, which suggest that the C-terminal part remains associated with FD until they both reach the viral membrane (Libersou et al., 2010; Si et al., 2018). Therefore, there is no evidence for an interaction between TM domains in the pre-fusion structure. Such an interaction would imply that the C-terminal segments of each protomer ectodomain are lying flat at the surface of the viral membrane and that they meet at the level of the first residues of the TM domain (Figure 7D). This cannot be excluded, because this is the case for the membrane proximal region of herpes simplex virus 1 (HSV-1) glycoprotein B (gB) in its post-fusion conformation (Cooper et al., 2018).

The Pair of Residues D280 and H389 Stabilizes the Post-Fusion State

The lateral chains of residues D280 and H389 face each other in the post-fusion state. They form a salt bridge between the negatively charged carboxylate and the positively charged imidazole groups in a hydrophobic environment, which contributes to the pH-dependent stability of the central 6-helix bundle.

The D280L mutation strongly affects VSV-G fusion properties. Its introduction in the viral genome resulted in the immediate selection of the H389L compensatory mutation. However, mutant H389A does not affect fusion activity and the corresponding recombinant VSV is only slightly affected. Globally, if we consider the pair of residues in position 280 and 389 that have been analyzed, pairs D/A, D/L, and L/L result in a G with fusion activity similar to that of WT. The only non-functional pair is the L/H one. In this pair, the lateral chain of the leucine would come into close contact with the imidazole group, whereas in pairs D/A and D/L, the hydrophobic side chain in position 389 is farther from the carboxylate group of the aspartate residue.

H407: A Key Player in the Structural Transition

The H407A mutation strongly affects G fusion properties. In the pre-fusion state, H407 is in the middle of a cluster of histidines (60, 162, 407, and 409) and serines. In this cluster (Figure 1A), several hydrogen bonds between histidines and serines and between histidines themselves stabilize the pre-fusion structure that is disrupted upon low-pH-induced histidine protonation. Among those histidines, only H60 and H407 are conserved in the *Vesiculovirus* genus and only H407 (which also contributes to the stabilization of the post-fusion protomer by making a salt bridge with D137) is conserved beyond the *Vesiculovirus* genus (at least in the *Perhabdovirus, Sprivirus, Novirhabdovirus,* and *Lyssavirus* genera) (Belot et al., 2020). In line with this, mutations of the other histidines of the cluster into alanines do not affect the fusion properties.

At the cell surface, mutant H407A poorly binds the LDL-R CR3 domain. Residue 407 is far from the CR binding site on G. This indicates that the equilibrium between the states is shifted toward G conformations that are unable to recognize CR3, i.e., distinct from the pre-fusion protomer and EI (on which the CR binding site is still present) (Baquero et al., 2017; Nikolic et al., 2018). Therefore, the H407A mutation destabilizes the pre-fusion state. However, it does not seem to affect the G ability to transit toward the post-fusion state (as judged by analysis of the G oligomeric state in the sucrose gradient and EM).

The compensatory mutations of H407A are located at positions distant from H407. The first one is in position 396. In the pre-fusion state, L396 is in a hydrophobic pocket made by Leu 374, Leu 392, Met 386, Ile 387, and Val 300 (Figure 7E). It stabilizes the kink made by the polypeptide chain at the level of Gly 390 and positions the downstream segment (398–404) in the groove of TrD (Figure 7F). In the post-fusion state, L396 is part of the lateral helix (residues 384–400) of the central six-helix bundle; it is also in a hydrophobic environment and interacts with Leu 392 in the same helix, Val 269 and Ile 272 of the central helix in the same protomer, and Leu 271 of a neighbor protomer (Figure 7G). The replacement of L396 by an isoleucine (in the context of H407A mutation) stabilizes the pre-fusion state, because the double mutant L396I/H407A binds CR3 more efficiently than H407A.

The second compensatory mutation is in position 422. In the pre-fusion structure, residue S422 points toward F424 and L430. The S422I compensatory mutation should stabilize the β-hairpin structure through the formation of a cluster of

Figure 5. Characterization of the Properties of Recombinant Viruses VSV-G.H389A, VSV-G.D280L/H389L, VSV-G.H407A/S422I, and VSV-G.L396I/H407A

(A) One-step growth curves of WT VSV, VSV-G.H389A, VSV-G.D280L/H389L, VSV-G.H407A/S422I, and VSV-G.L396I/H407A. BSR cells were infected at an MOI of 3, and samples were harvested for titration at the indicated times post-infection. Viral titers represent averages of titers from at least three independent experiments (error bars correspond to standard deviation).

(B) Expression and subcellular localization of mutant G proteins in BSR cells after transfection. Epifluorescence images of transfected cells are shown. Experiments were performed as described in the legend of Figure 2A.

(C) Flow cytometry analysis of the expression of WT and mutant G at the surface of HEK293T cells. In each frame, the black curve corresponds to the fluorescence of untransfected cells, the blue curve corresponds to the fluorescence of cells transfected by pCAGGS plasmids encoding WT G, and the red curve corresponds to the fluorescence of cells transfected by pCAGGS plasmids encoding the indicated mutant. Experiments were performed as described in the legend of Figure 2B.

(D) Flow cytometry analysis of the expression of WT and mutant G at the surface of HEK293T cells and of the binding of fluorescent GST-CR3. Experiments were performed as described in the legend of Figure 4A.

(E) Quantification of surface expression and CR3 binding properties of mutant G expressed in HEK293T cells. The surface expression (in blue) is expressed as a percentage of that of WT G. The percentage of cells expressing G that are also positive for CR3 is in orange. Values are the average of at least 3 independent experiments (like the one presented in C) ± the standard deviation. Statistically significant differences with WT are indicated by black stars and with H407A are indicated by red ones (*$p < 0.05$, **$p < 0.005$, ***$p < 0.0005$).

(F) Fusion activity of WT and VSV-G mutants analyzed in a cell-cell fusion assay. Experiments were performed as described in the legend of Figure 3. All images are representative examples from at least three independent experiments.

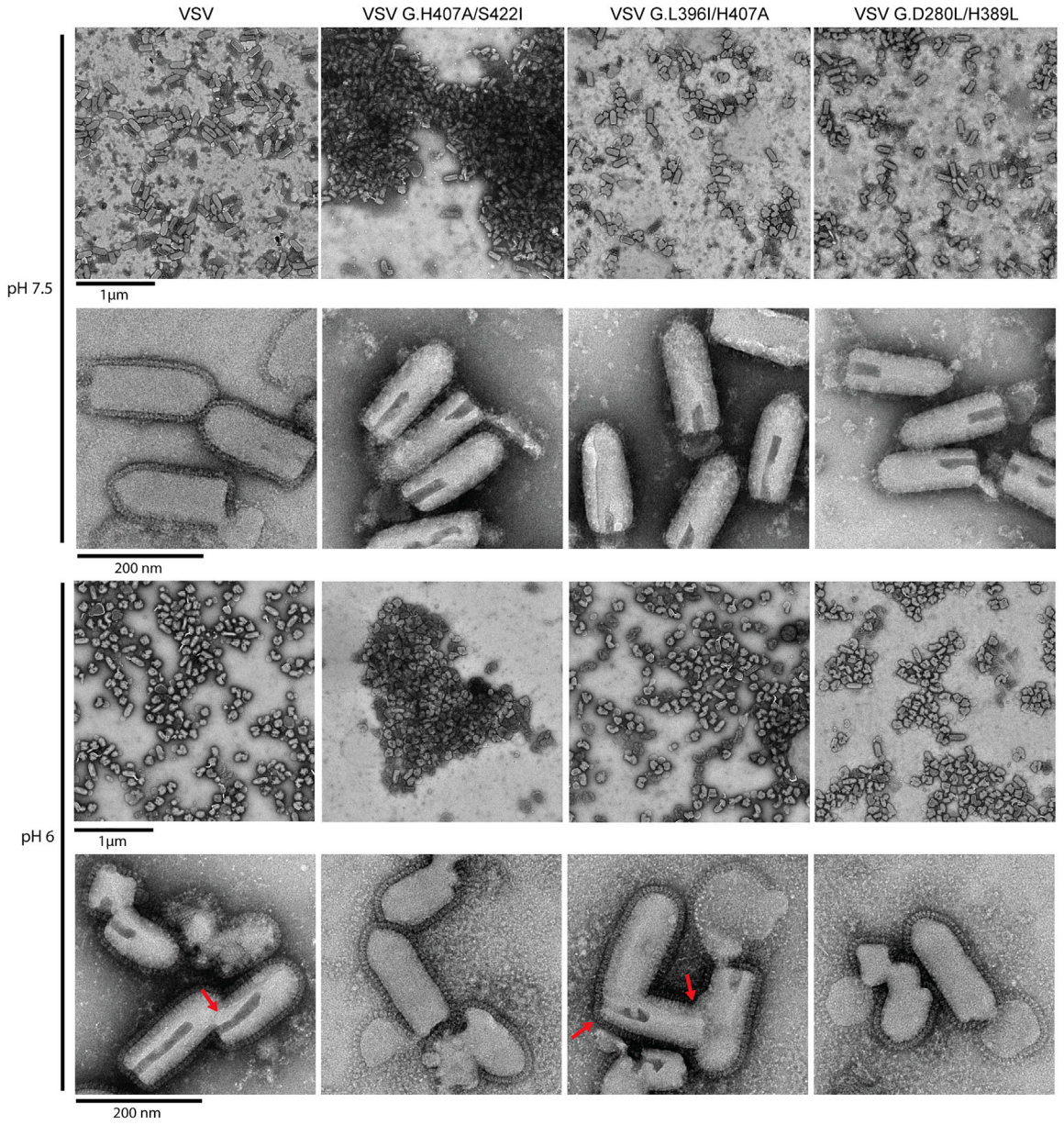

Figure 6. Morphology of Negatively Stained WT and Mutant VSV at pH 7.5 and 6

For each mutant, at each pH, a wide field is presented (top row), together with higher-magnification micrographs (bottom row) revealing the details of the virions. The wide fields at pH 7.5 reveal the aggregation tendency of mutant VSV-G.H407A/S422I. Individual virions reveal the typical pre-fusion layer of spikes at pH 7.5 and the typical post-fusion trimer at pH 6. Red arrows indicate virions that have fused at pH 6.

hydrophobic residues and thus the pre-fusion state (Figure 7H). Indeed, the double mutant H407A/S422I binds CR3 significantly more than H407A. Nevertheless, CR3 binding by H407A/S422I appears reduced when compared with WT. This suggests that for mutant H407A/S422I, the equilibrium is still shifted toward G states that are unable to bind CR domains. This is corroborated by the massive virion aggregation at pH 7.5 that, with WT VSV and RABV, is generally observed at lower pH when the Gs at the viral surface adopt intermediate conformations that expose the fusion loops (Gaudin et al., 1993; Libersou et al., 2010).

Implications on the Pathway of the Conformational Change

The determination of intermediate structures during the conformational change of CHAV-G (Baquero et al., 2017) has suggested that contrary to the previously proposed model in which the transition was initiated by a movement of FD (Harrison, 2015; Roche et al., 2007), the first rearrangement in the structure takes place in the C-terminal part of the ectodomain. The data presented here are in agreement with this scenario. The intimate interaction between the C-terminal domain, which refolds during

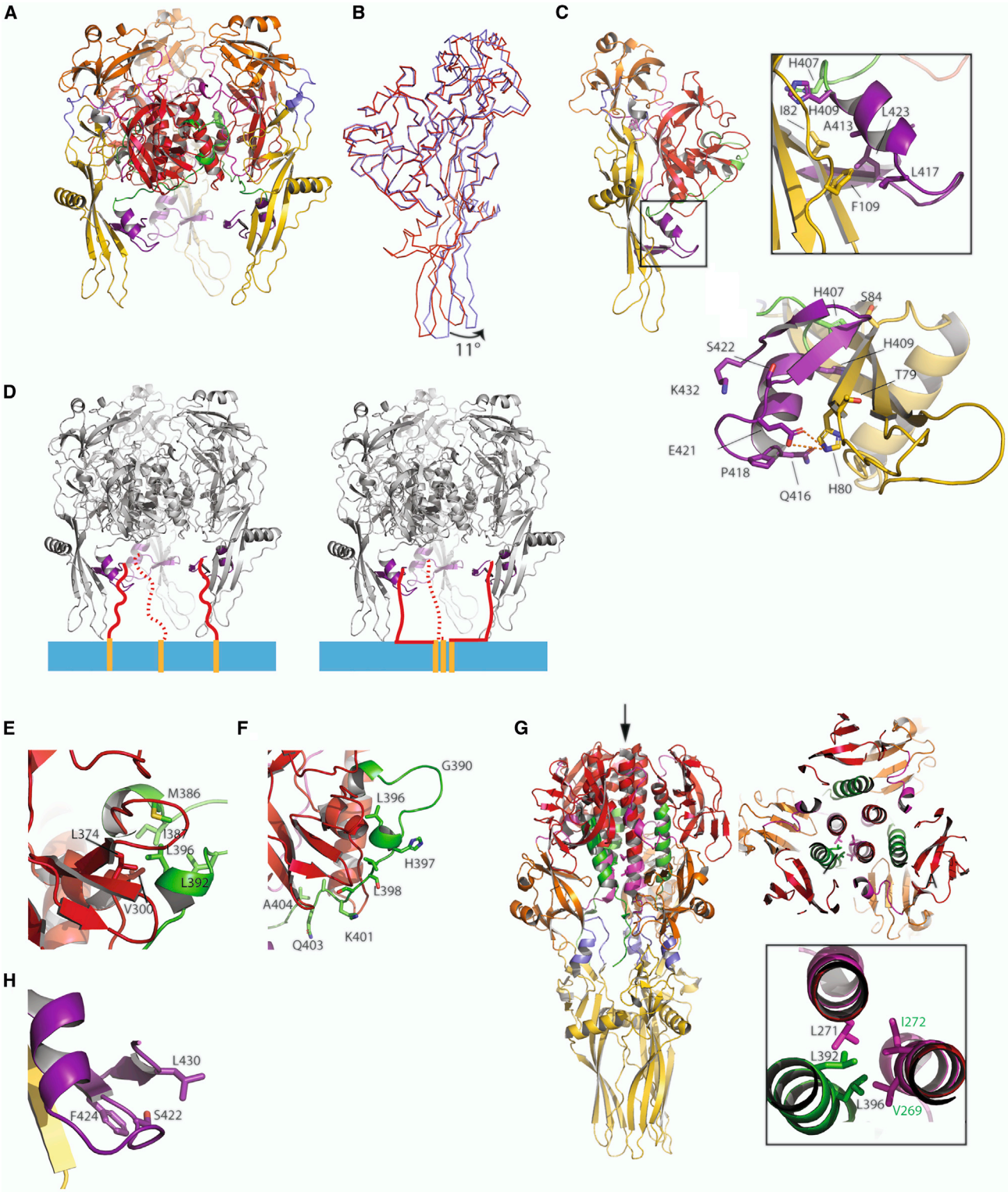

Figure 7. Crystal Structure of $G_{1–440}$ and Environment of Residues L396 and S422

(A) Crystalline structure of the pre-fusion trimer of $G_{1–440}$. The chain is traced up to residue 432. Residues 410 to 432 are in purple.

(B) Superimposition of the G_{th} and $G_{1–440}$ pre-fusion protomers after alignment on residues 1 to 63 and 127 to 410 showing the 11° tilt of FD.

(C) Structure of segment 410–432. The two close-ups detail the organization of segment 410–432 and its interactions with FD.

(legend continued on next page)

the transition, and FD, which keeps its conformation, makes difficult a movement of the latter without a conformational change of the former.

Furthermore, the compensatory mutation of both S422I and L396I stabilizes the pre-fusion state without interacting with FD or the hinge regions R2 and R3. As mentioned earlier, S422I clearly stabilizes the pre-fusion C-terminal hairpin structure through the formation of a cluster of hydrophobic residues. Similarly, an isoleucine in position 396 probably anchors the residue in its pre-fusion hydrophobic pocket more efficiently than a leucine, thus stabilizing the pre-fusion conformation. Therefore, the R5 segment is leaving the TrD groove it occupies in the pre-fusion conformation and detaches from FD before any other structural change. This confers mobility to the rest of the G ectodomain and allows orientation of the fusion loops toward the target membrane to initiate the fusion process.

STAR★METHODS

Detailed methods are provided in the online version of this paper and include the following:

- KEY RESOURCES TABLE
- RESOURCE AVAILABILITY
  - Lead Contact
  - Materials Availability
  - Data and Code Availability
- EXPERIMENTAL MODEL AND SUBJECT DETAILS
  - Cell lines
  - Virus
- METHOD DETAILS
  - Antibodies
  - Plasmids and cloning
  - Transfections
  - Indirect immunofluorescence
  - Cell surface expression
  - Cell-cell fusion assay
  - Oligomerization assay
  - Recovery of recombinant virus
  - Binding of CR3-GST to cells expressing WT or mutant G
  - Preparation of pseudotypes
  - Virus purification for EM
  - Electron microscopy
  - $G_{1\text{-}440}$ expression and crystallization
  - Structure determination and refinement
- QUANTIFICATION AND STATISTICAL ANALYSIS

SUPPLEMENTAL INFORMATION

Supplemental Information can be found online at https://doi.org/10.1016/j.celrep.2020.108042.

ACKNOWLEDGMENTS

This work was supported by grants from the Fondation pour la Recherche Médicale, France, (FRM DEQ20120323711) (including a post-doctoral grant to F.B.) and from the Agence Nationale de la Recherche, France, (ANR CE11 MOBARHE) to Y.G. (including a post-doctoral grant to A.A.H.). We acknowledge the European Synchrotron Radiation Facility (Grenoble, France) and synchrotron SOLEIL (Saint-Aubin, France) for providing radiation facilities. We acknowledge the structural biology pole of the IMAGIF integrated platform (https://www.i2bc.paris-saclay.fr/spip.php?rubrique184&lang=en) for access to crystallization and EM facilities. The work was financially supported by the French Infrastructure for Integrated Structural Biology Initiative ([FRISBI] ANR-10-INSB-05-02)

AUTHOR CONTRIBUTIONS

F.B., A.A.H., H.R., L.B., M.O., and A.A.A. conducted the experiments. F.B. and H.R. performed mutagenesis and characterized the mutant's properties. A.A.H. expressed $G_{1\text{–}440}$, collected X-ray diffraction data, and solved and refined the $G_{1\text{–}440}$ structure. L.B. collected X-ray data and performed CR binding experiments. A.A.A. characterized the oligomeric status of mutant H407A. M.O. performed EM. A.A.A. supervised the structural part of the work. Y.G. supervised the study. F.B., A.A.H., and L.B. participated in manuscript editing and discussion. A.A.A. and Y.G. wrote the manuscript.

DECLARATION OF INTERESTS

The authors declare no competing interests.

Received: November 22, 2019
Revised: July 12, 2020
Accepted: July 24, 2020
Published: August 18, 2020

REFERENCES

Afonine, P.V., Grosse-Kunstleve, R.W., Echols, N., Headd, J.J., Moriarty, N.W., Mustyakimov, M., Terwilliger, T.C., Urzhumtsev, A., Zwart, P.H., and Adams, P.D. (2012). Towards automated crystallographic structure refinement with phenix.refine. Acta Crystallogr. D Biol. Crystallogr. *68*, 352–367.

Albertini, A.A., Mérigoux, C., Libersou, S., Madiona, K., Bressanelli, S., Roche, S., Lepault, J., Melki, R., Vachette, P., and Gaudin, Y. (2012a). Characterization of monomeric intermediates during VSV glycoprotein structural transition. PLoS Pathog. *8*, e1002556.

Albertini, A.A.V., Baquero, E., Ferlin, A., and Gaudin, Y. (2012b). Molecular and cellular aspects of rhabdovirus entry. Viruses *4*, 117–139.

Backovic, M., and Krey, T. (2016). Stable *Drosophila* Cell Lines: An Alternative Approach to Exogenous Protein Expression. Methods Mol. Biol. *1350*, 349–358.

(D) Alternative localization of the TM domains in agreement with the EM envelopes obtained by tomography. In the left structure, the TM domains are located below FD and do not associate. In the right structure, the C-terminal segments of the ectodomains are lying flat at the surface and gather at the center of the structure, thus bringing together the TM domains.
(E) L396 is located in a hydrophobic pocket in the G pre-fusion state.
(F) Close-up view of segment 390–404 placed in the groove of TrD in the G pre-fusion state (in red).
(G) Environment of residue L396 in the post-fusion six-helix bundle. In the close-up view, residues belonging to different chains are labeled in different colors (black and green).
(H) Close-up view of residue S422 in the G pre-fusion state.
The color code in (A),(C), and (E)–(H) is the same as in Figure 1; segment 410–432 is in purple.

Baquero, E., Albertini, A.A., and Gaudin, Y. (2015). Recent mechanistic and structural insights on class III viral fusion glycoproteins. Curr. Opin. Struct. Biol. *33*, 52–60.

Baquero, E., Albertini, A.A., Raux, H., Abou-Hamdan, A., Boeri-Erba, E., Ouldali, M., Buonocore, L., Rose, J.K., Lepault, J., Bressanelli, S., and Gaudin, Y. (2017). Structural intermediates in the fusion-associated transition of vesiculovirus glycoprotein. EMBO J. *36*, 679–692.

Belot, L., Ouldali, M., Roche, S., Legrand, P., Gaudin, Y., and Albertini, A.A. (2020). Crystal structure of Mokola virus glycoprotein in its post-fusion conformation. PLoS Pathog. *16*, e1008383.

Carneiro, F.A., Stauffer, F., Lima, C.S., Juliano, M.A., Juliano, L., and Da Poian, A.T. (2003). Membrane fusion induced by vesicular stomatitis virus depends on histidine protonation. J. Biol. Chem. *278*, 13789–13794.

Charafeddine, R.A., Cortopassi, W.A., Lak, P., Tan, R., McKenney, R.J., Jacobson, M.P., Barber, D.L., and Wittmann, T. (2019). Tau repeat regions contain conserved histidine residues that modulate microtubule-binding in response to changes in pH. J. Biol. Chem. *294*, 8779–8790.

Cooper, R.S., Georgieva, E.R., Borbat, P.P., Freed, J.H., and Heldwein, E.E. (2018). Structural basis for membrane anchoring and fusion regulation of the herpes simplex virus fusogen gB. Nat. Struct. Mol. Biol. *25*, 416–424.

Doms, R.W., Keller, D.S., Helenius, A., and Balch, W.E. (1987). Role for adenosine triphosphate in regulating the assembly and transport of vesicular stomatitis virus G protein trimers. J. Cell Biol. *105*, 1957–1969.

Emsley, P., Lohkamp, B., Scott, W.G., and Cowtan, K. (2010). Features and development of Coot. Acta Crystallogr. D Biol. Crystallogr. *66*, 486–501.

Ferlin, A., Raux, H., Baquero, E., Lepault, J., and Gaudin, Y. (2014). Characterization of pH-sensitive molecular switches that trigger the structural transition of vesicular stomatitis virus glycoprotein from the postfusion state toward the prefusion state. J. Virol. *88*, 13396–13409.

Finkelshtein, D., Werman, A., Novick, D., Barak, S., and Rubinstein, M. (2013). LDL receptor and its family members serve as the cellular receptors for vesicular stomatitis virus. Proc. Natl. Acad. Sci. USA *110*, 7306–7311.

Fritz, R., Stiasny, K., and Heinz, F.X. (2008). Identification of specific histidines as pH sensors in flavivirus membrane fusion. J. Cell Biol. *183*, 353–361.

Gaudin, Y. (2000). Reversibility in fusion protein conformational changes. The intriguing case of rhabdovirus-induced membrane fusion. Subcell. Biochem. *34*, 379–408.

Gaudin, Y., Ruigrok, R.W., Knossow, M., and Flamand, A. (1993). Low-pH conformational changes of rabies virus glycoprotein and their role in membrane fusion. J. Virol. *67*, 1365–1372.

Harrison, S.C. (2015). Viral membrane fusion. Virology *479–480*, 498–507.

Jeetendra, E., Ghosh, K., Odell, D., Li, J., Ghosh, H.P., and Whitt, M.A. (2003). The membrane-proximal region of vesicular stomatitis virus glycoprotein G ectodomain is critical for fusion and virus infectivity. J. Virol. *77*, 12807–12818.

Kabsch, W. (2010). Xds. Acta Crystallogr. D Biol. Crystallogr. *66*, 125–132.

Kim, I.S., Jenni, S., Stanifer, M.L., Roth, E., Whelan, S.P., van Oijen, A.M., and Harrison, S.C. (2017). Mechanism of membrane fusion induced by vesicular stomatitis virus G protein. Proc. Natl. Acad. Sci. USA *114*, E28–E36.

Krissinel, E., and Henrick, K. (2004). Secondary-structure matching (SSM), a new tool for fast protein structure alignment in three dimensions. Acta Crystallogr. D Biol. Crystallogr. *60*, 2256–2268.

Lawson, N.D., Stillman, E.A., Whitt, M.A., and Rose, J.K. (1995). Recombinant vesicular stomatitis viruses from DNA. Proc. Natl. Acad. Sci. USA *92*, 4477–4481.

Libersou, S., Albertini, A.A., Ouldali, M., Maury, V., Maheu, C., Raux, H., de Haas, F., Roche, S., Gaudin, Y., and Lepault, J. (2010). Distinct structural rearrangements of the VSV glycoprotein drive membrane fusion. J. Cell Biol. *191*, 199–210.

Mair, C.M., Meyer, T., Schneider, K., Huang, Q., Veit, M., and Herrmann, A. (2014). A histidine residue of the influenza virus hemagglutinin controls the pH dependence of the conformational change mediating membrane fusion. J. Virol. *88*, 13189–13200.

Munis, A.M., Tijani, M., Hassall, M., Mattiuzzo, G., Collins, M.K., and Takeuchi, Y. (2018). Characterization of Antibody Interactions with the G Protein of Vesicular Stomatitis Virus Indiana Strain and Other Vesiculovirus G Proteins. J. Virol. *92*, e00900-18.

Nikolic, J., Belot, L., Raux, H., Legrand, P., Gaudin, Y., and Albertini, A.A. (2018). Structural basis for the recognition of LDL-receptor family members by VSV glycoprotein. Nat. Commun. *9*, 1029.

Pasdeloup, D., Poisson, N., Raux, H., Gaudin, Y., Ruigrok, R.W., and Blondel, D. (2005). Nucleocytoplasmic shuttling of the rabies virus P protein requires a nuclear localization signal and a CRM1-dependent nuclear export signal. Virology *334*, 284–293.

Roche, S., and Gaudin, Y. (2002). Characterization of the equilibrium between the native and fusion-inactive conformation of rabies virus glycoprotein indicates that the fusion complex is made of several trimers. Virology *297*, 128–135.

Roche, S., Bressanelli, S., Rey, F.A., and Gaudin, Y. (2006). Crystal structure of the low-pH form of the vesicular stomatitis virus glycoprotein G. Science *313*, 187–191.

Roche, S., Rey, F.A., Gaudin, Y., and Bressanelli, S. (2007). Structure of the prefusion form of the vesicular stomatitis virus glycoprotein G. Science *315*, 843–848.

Rozo-Lopez, P., Drolet, B.S., and Londoño-Renteria, B. (2018). Vesicular Stomatitis Virus Transmission: A Comparison of Incriminated Vectors. Insects *9*, 190.

Schnell, M.J., Buonocore, L., Whitt, M.A., and Rose, J.K. (1996). The minimal conserved transcription stop-start signal promotes stable expression of a foreign gene in vesicular stomatitis virus. J. Virol. *70*, 2318–2323.

Si, Z., Zhang, J., Shivakoti, S., Atanasov, I., Tao, C.L., Hui, W.H., Zhou, K., Yu, X., Li, W., Luo, M., et al. (2018). Different functional states of fusion protein gB revealed on human cytomegalovirus by cryo electron tomography with Volta phase plate. PLoS Pathog. *14*, e1007452.

Srivastava, J., Barber, D.L., and Jacobson, M.P. (2007). Intracellular pH sensors: design principles and functional significance. Physiology (Bethesda) *22*, 30–39.

Stanifer, M.L., Cureton, D.K., and Whelan, S.P. (2011). A recombinant vesicular stomatitis virus bearing a lethal mutation in the glycoprotein gene uncovers a second site suppressor that restores fusion. J. Virol. *85*, 8105–8115.

Sun, X., Belouzard, S., and Whittaker, G.R. (2008). Molecular architecture of the bipartite fusion loops of vesicular stomatitis virus glycoprotein G, a class III viral fusion protein. J. Biol. Chem. *283*, 6418–6427.

Svensson, O., Gilski, M., Nurizzo, D., and Bowler, M.W. (2018). Multi-position data collection and dynamic beam sizing: recent improvements to the automatic data-collection algorithms on MASSIF-1. Acta Crystallogr. D Struct. Biol. *74*, 433–440.

Vagin, A., and Teplyakov, A. (2010). Molecular replacement with MOLREP. Acta Crystallogr. D Biol. Crystallogr. *66*, 22–25.

Vercoulen, Y., Kondo, Y., Iwig, J.S., Janssen, A.B., White, K.A., Amini, M., Barber, D.L., Kuriyan, J., and Roose, J.P. (2017). A Histidine pH sensor regulates activation of the Ras-specific guanine nucleotide exchange factor RasGRP1. eLife *6*, e29002.

Williamson, D.M., Elferich, J., and Shinde, U. (2015). Mechanism of Fine-tuning pH Sensors in Proprotein Convertases: IDENTIFICATION OF A pH-SENSING HISTIDINE PAIR IN THE PROPEPTIDE OF PROPROTEIN CONVERTASE 1/3. J. Biol. Chem. *290*, 23214–23225.

Wu, W., Celma, C.C., Kerviel, A., and Roy, P. (2019). Mapping the pH Sensors Critical for Host Cell Entry by a Complex Nonenveloped Virus. J. Virol. *93*, e01897-18.

Yang, F., Lin, S., Ye, F., Yang, J., Qi, J., Chen, Z., Lin, X., Wang, J., Yue, D., Cheng, Y., et al. (2020). Structural Analysis of Rabies Virus Glycoprotein Reveals pH-Dependent Conformational Changes and Interactions with a Neutralizing Antibody. Cell Host Microbe *27*, 441–453.

Zagouras, P., and Rose, J.K. (1993). Dynamic equilibrium between vesicular stomatitis virus glycoprotein monomers and trimers in the Golgi and at the cell surface. J. Virol. *67*, 7533–7538.

STAR★METHODS

KEY RESOURCES TABLE

REAGENT or RESOURCE	SOURCE	IDENTIFIER
Antibodies		
Mouse monoclonal antibody 8G5F11 against G ectodomain	KERAFAST	Cat#EB0010
Mouse monoclonal antibody P5D4 against the C-terminal intraviral part of G	SIGMA Aldrich	Cat# V5507; RRID:AB_261877
Bacterial and Virus Strains		
VSV (Indiana Mudd-Summer strain)	Gaudin's lab	N/A
VSVΔG-GFP	Gaudin's lab	N/A
E. Coli strain C41(DE3)	Lucigen	Cat# 60441-1
Chemicals, Peptides, and Recombinant Proteins		
Lipofectamine 2000 transfection Reagent	Invitrogen	Cat# 11668019
Polyethylenimine (PEIMax)	Polyscience	Cat# 24765-1
Protein A-magnetic beads	New England Biolab	Cat# S1425S
ATTO550 NHS ester	SIGMA Aldrich	Cat# 30730
L-α-Phosphatidylcholine from egg yolk, Type XVI-E,	SIGMA Aldrich	P3556
L-α-Phosphatidylethanolamine from Glycine max (soybean), Type IV	SIGMA Aldrich	P8193
Total ganglioside extract, brain porcine, ammonium salt	AVANTI Polar Lipids	960053P
Deposited Data		
Atomic model of VSV G_{1-440}	This paper	PDB: 6TIT
Experimental Models: Cell Lines		
BSR cells, clones of BHK-21	Gaudin's lab	
HEK293T	ATCC	CRL-3216
S2 Drosophila Schneider cells	GIBCO	Cat# R69007
Recombinant DNA		
pCAGGS plasmids encoding the WT G or mutant	This paper	N/A
pT350 vector encoding G_{1-440}	This paper	N/A
Software and Algorithms		
MOLREP	Vagin and Teplyakov, 2010	http://www.ccp4.ac.uk/html/molrep.html
COOT	Emsley et al., 2010	https://www2.mrc-lmb.cam.ac.uk/personal/pemsley/coot/
PHENIX	Afonine et al., 2012	https://www.phenix-online.org/
PyMOL Molecular Graphics System	DeLano Scientific LLC	https://pymol.org/2/
Other		
Tangential filtration unit Vivaflow 200	SARTORIUS	Cat# 147013

RESOURCE AVAILABILITY

Lead Contact

Further information and requests for resources and reagents should be directed to and will be fulfilled by the Lead Contact, Yves Gaudin (yves.gaudin@i2bc.paris-saclay.fr).

Materials Availability

All unique/stable reagents generated in this study are available from the Lead Contact with a completed Uniform Biological Materials Transfer Agreement.

Data and Code Availability

The accession number for the atomic coordinates and structure factors reported in this paper is PDB: 6TIT.

EXPERIMENTAL MODEL AND SUBJECT DETAILS

Cell lines

BSR, clones of BHK-21 (baby hamster kidney; ATCC CCL-10), and HEK293T (human embryonic kidney expressing simian virus 40 T antigen [SV40T]; ATCC CRL-3216) cells were grown in Dulbecco's modified Eagle's medium (DMEM) supplemented with 8% fetal calf serum (FCS). S2 *Drosophila* Schneider cells (GIBCO, Cat# R69007) were grown in Express Five media (GIBCO, Cat# 10486025) supplemented with 20 mM L-glutamine and 7μg/ml puromycin.

Virus

VSV Indiana Mudd-Summer strain was propagated in BSR cells.

METHOD DETAILS

Antibodies

Mouse monoclonal antibody directed against G ectodomain was supplied by KeraFAST (8G5F11); mouse monoclonal antibody directed against the C-terminal intraviral part of G was supplied by Sigma (P5D4).

Plasmids and cloning

Point mutations were created starting from the cloned VSV G gene (Indiana Mudd-Summer strain) in the pCAGGS plasmid. Briefly, forward and reverse primers containing the desired mutation were combined separately with one of the primers flanking the G gene to generate two PCR products. These two G gene fragments overlap in the region containing the mutation and were assembled into the pCAGGS linearized vector using Gibson assembly reaction kit (New England Biolabs). For stable expression in S2 cells, the ectodomain sequence VSV $G_{1\text{-}440}$ was subcloned into the expression vector pT350 using Gibson assembly reaction kit (New England Biolabs) so that VSV G ectodomain is flanked by the *Drosophila* Bip secretion signal at the N terminus and an enterokinase-cleavable double StrepTag at the C terminus (sequence: DDDDKAGWSHPQFEKGGGSGGGSGGGSWSHPQFEK).

Transfections

For fusion assays and indirect immunofluorescence, BSR cells, grown in six-well plates at 70% confluence, were transfected by the calcium phosphate method (5 μg of the appropriate plasmid per well).

For G sedimentation analysis and cytometry experiments, HEK293T cells grown in six-well plates at 70 to 80% confluence were transfected with 2 μg of the appropriate plasmid using Lipofectamine 2000 (Invitrogen) according to the manufacturer's instructions.

For pseudotyped virus production, HEK293T cells were grown in 10-cm dishes; they were transfected by 6 μg of the appropriate plasmid mixed with 30μl of polyethylenimine (PEIMax; Polyscience) at 1mg/ml.

Indirect immunofluorescence

BSR cells plated on glass coverslips at 70% confluence were transfected with pCAGGS plasmids encoding WT or mutant G, as described above. At 24 h after transfection, cells were fixed with 4% paraformaldehyde in phosphate-buffered saline (PBS) for 15 min and then permeabilized or not in 0.1% Triton X-100 in PBS for 5 min. Glycoprotein was detected by using a mouse monoclonal anti-G ectodomain antibody (8G5F11; KeraFAST). Goat anti-mouse Alexa Fluor 488 (Invitrogen) was used as a secondary antibody. Images were acquired with a Zeiss Axiovert 200 fluorescence microscope (Carl Zeiss MicroImaging, Inc., Germany) equipped with a 63 × lens (oil) connected to a charge-coupled-device camera and a computer equipped with AxioVision software. Excitation was performed at 488 nm (Alexa Fluor 488). Cell nuclei were stained with 4′,6′-diamidino-2-phenylindole (DAPI).

Cell surface expression

To quantify the expression of G protein on the cell surface, HEK293T cells plated on six-well dishes at 70% confluence were transfected as described above. At 24 h after transfection, cells were collected by scraping into 1 mM EDTA-PBS, followed by centrifugation at 600 g for 5 min. Cells were incubated with a 1:2,000 dilution of mouse monoclonal anti-G ectodomain antibody (8G5F11; KeraFAST) in PBS on ice for 1 h. Cells were washed twice in PBS, fixed at 4°C in paraformaldehyde, incubated with a 1:1000 dilution of goat anti-mouse Alexa Fluor 488 (Invitrogen) on ice for 1 h, and rinsed in PBS. After resuspension in 500 μl of 0.5 mM EDTA-PBS, the fluorescence of 10,000 cells from each population was determined by flow cytometry using a BD Accuri C6 flow cytometer. The mean fluorescence intensity (MFI) of the transfected cells expressing G was quantified by flow cytometry. The relative cell surface expression of transfected cells was determined as follows: (MFI for the mutant)/(MFI for the WT). For each mutant, the percentage given in Figures 2, 4, and 5 is the average of at least three independent experiments.

Cell-cell fusion assay

BSR cells plated on glass coverslips at 70% confluence were cotransfected with pCAGGS plasmids encoding the WT G or mutant G and a plasmid encoding the phosphoprotein of rabies virus fused to the green fluorescent protein (P-GFP) (Pasdeloup et al., 2005). At 24 h after transfection, cells were incubated with fusion buffer (DMEM 10 mM morpholineethanesulfonic acid [MES]) at various pHs (from 5.0 to 7.0) for 10 min at 37°. Cells were then washed once and incubated with DMEM–10 mM HEPES–NaOH buffered at pH 7.4 and 8% bovine serum albumin (BSA) at 37°C for 1 h. Cells were fixed with 4% paraformaldehyde in PBS for 15 min. Cell nuclei were stained with DAPI, and syncytium formation was analyzed with a Zeiss Axiovert 200 fluorescence microscope equipped with a 20 × lens.

Oligomerization assay

The oligomeric state of G was determined by sucrose gradient centrifugation. HEK293T cells were transfected by the Lipofectamine method as described above. At 24 h after transfection, cells were collected by scraping into PBS, followed by centrifugation at 2,500 rpm for 5 min. Cell lysates were prepared using 100 mM NaCl containing either 50 mM MES-NaOH (for pH 5 to 6.5) or 50 mM Tris-HCl (for pH 7 and 7.5) plus 0.5% NP-40 at 4°C for 30 min; they were clarified by centrifugation at 10,000 rpm for 2 min and overlaid on a 5 to 20% continuous sucrose gradient in 100 mM NaCl and 50 mM Tris-HCl pH 7.0 or 100 mM NaCl and 50 mM MES-NaOH [pH 6.0 or 6.5], plus 0.1% Triton supplemented with a antiprotease cocktail (Roche). After ultracentrifugation at 35,000 rpm for 16 h in a sw41 rotor, 12 equal fractions of 1ml were collected from the bottom of the gradient. For low-expression mutant (H407A), the totality of G in each collected fraction was immunoprecipited, For this, the pH of each collected fraction was adjusted to 7.5, and G was immunoprecipitated using a mouse monolonal anti-G antibody 8G5F11 at 4°C for 2 h; immune complexes were immobilized on protein A-magnetic beads (NEB) for 1 h at 4°C, washed three times, denatured, and analyzed by SDS-PAGE. Immunoprecipitated G was revealed by Western immunoblotting with mouse monoclonal anti-G antibody P5D4.

For WT G, immunoprecipitation was not necessary. Twenty microliters of each collected fraction were analyzed by SDS-PAGE and revealed by western blot with a mouse monoclonal anti-G antibody P5D4.

Recovery of recombinant virus

Plasmid pVSV-FL(+) expressing the 11,161-nucleotide (nt) positive-strand full-length VSV RNA sequence and plasmids pBS-N, pBS-P, and pBS-L, respectively, encoding N, P, and L proteins were kindly provided by John K. Rose (Yale University, New Haven, CT, USA). The mutant G genes of the VSV Indiana serotype (Mudd-Summers strain) were inserted into the original full-length genomic plasmid pVSV-FL(+) (Lawson et al., 1995) using two unique restriction sites in pVSVFL(+), MluI in the 5′ noncoding sequence of the glycoprotein (G) gene and NheI present in a sequence introduced between G and L genes, after removal of the corresponding VSV Indiana Mudd-Summers G gene. Recombinant VSV was recovered in BSR cells as described by Schnell et al. (1996). BSR cells were infected with recombinant vaccinia virus expressing bacteriophage T7 RNA polymerase (vTF7-3) at a multiplicity of infection of 10. After 1 h, BSR cells were co-transfected with the pVSV-FL(+), pBS-N, pBS-P, and pBS-L plasmids using Lipofectamine 2000 (Invitrogen) in the presence of 10 μg/ml 1-β-d-arabinofuranosylcytosine (araC; Sigma).

Two mutants (VSV G.H407A and VSV G.D280L) could not be generated spontaneously. The recovery of these mutants was supported by the expression of functional WT VSV G protein in *trans* from a plasmid (pcDNA3.1 G WT) which was cotransfected with plasmids pVSV-FL(+), pBS-N, pBS-P, and pBS-L.

Binding of CR3-GST to cells expressing WT or mutant G

CR3-GST was produced in E. Coli (C41(DE3) strain from Lucigen) and labeled with the fluorescent dye ATTO550 NHS ester (Sigma Aldrich) using the instruction of the manufacturer, as previously described (Nikolic et al., 2018). The labeled proteins were then diluted at a concentration of 50 μM and stored at −80 °C until use. The labeling ratio was estimated to be around 2 dyes per molecule.

For flow cytometry experiments, HEK293T cells were transfected with pCAGGS plasmids encoding WT or mutant G using polyethylenimine. 24 h after transfection, cells were collected and incubated with mouse-monoclonal anti-G antibody 8G5F11 at a dilution of 1/1000. Goat anti-mouse Alexa fluor 488 (at a dilution of 1/1000) and GST-CR3^{ATTO550} at a concentration of 0.5 μM were then simultaneously added to the cells. The fluorescence of cells was measured using a BD Accuri C6 flow cytometer.

Preparation of pseudotypes

HEK293T cells at 80% confluence were transfected by pCAGGS encoding WT or mutant H407A VSV G using PEI Max (Polyscience). Twenty-four hours after transfection, cells were infected with VSVΔG-GFP and pseudotyped with VSV G WT at an MOI of 1. At two hours p.i., cells were washed to remove residual viruses from the inoculum. Cell supernatants containing the pseudotyped viral particles were collected at 16 h.p.i. Viral particles were purified as described below.

Virus purification for EM

VSV was propagated in BSR cells. Sixteen hours post-infection, cell debris were eliminated from the supernatant by filtration; then the virus was pelleted by centrifugation at 4°C (45 min 25,000 rpm in a sw28 rotor) and gently re-suspended in TEM buffer (150 mM NaCl, 10 mM Tris-HCl pH 7.5, 2 mM EDTA).

Electron microscopy

Purified virions and pseudotypes were diluted in 150 mM NaCl, 50 mM Tris-HCl, pH 7.5, or dialyzed against a buffer containing 150 mM NaCl and 50 mM MES at pH 6 (or pH5.5). Samples were then adsorbed onto airglow discharge carbon-coated grids and stained with sodium phosphotungstic acid adjusted to the sample pH (7.5, 6 or 5.5).

Purified WT and mutant H407A VSV $G_{1\text{-}440}$ were diluted in 150 mM NaCl in 50 mM MES at pH 5.5 in the absence or presence of liposomes (PC/PE/gangliosides: 7/3/1) prepared as described in Libersou et al. (2010). The mixture was then adsorbed onto grids and stained with uranyl acetate (protein alone) or with sodium phosphotungstic acid (protein plus liposomes) adjusted to the sample pH.

Images were recorded in an electron microscope Tecnai Spirit 120 kV (FEI) with a GATAN K2 camera operated at 120 kV.

$G_{1\text{-}440}$ expression and crystallization

As explained by Backovic and Krey (2016), stable cell lines expressing VSV G ectodomain with a C-terminal tandem StrepTag were generated by cotransfecting S2 cells with a plasmid encoding VSV $G_{1\text{-}440}$ cloned in a pT350 vector and a plasmid encoding the puromycin resistance gene. To produce VSV $G_{1\text{-}440}$ in large quantities, S2 cells were grown in suspension at 28°C, 120 rpm until reaching a density of 1.5 10^7 cells/ml in media supplemented with 7μg/ml puromycin. The cell culture was then diluted twice and induced with 500 μM $CuSO_4$. The culture was harvested 5 days after induction and the supernatant was concentrated by tangential filtration (Vivaflow 200, Sartorius). VSV $G_{1\text{-}440}$ were purified thanks to their StrepTag on a streptavidin affinity column (Strep Trap HP, GE Healthcare) in a 20 mM Tris-HCl pH 8 buffer, 150 mM NaCl, 2 mM EDTA. Elution was carried out in the same buffer to which 3 mM α-Desthiobiotin was added. StrepTag removal was carried out for 16 h at 22°C in the presence of enterokinase after dilution of $G_{1\text{-}440}$ in 100 mM MES pH 6 buffer. Purification was achieved on a size exclusion chromatography (Superdex 200 increase column 10/300, GE Healthcare) equilibrated in 20mM Tris-HCl pH 8. Purified of $G_{1\text{-}440}$ were concentrated (Amicon Ultra 30kDa c/o, Millipore) and stored at −80°C.

$G_{1\text{-}440}$ crystals were obtained by the hanging-drop vapor diffusion method. Briefly, 1 μl of cleaved $G_{1\text{-}440}$ (5 mg/ml prepared in 20 mM Tris HCl pH 8, 150 mM NaCl), supplemented with 0.3% n-dodecyl β–D-maltoside (DDM) was mixed to 1 μl of the reservoir solution (8% PEG8000, 0.15 M calcium acetate, 0.15 M HEPES pH 7.5) and equilibrated against 1 mL of reservoir solution. Crystals were harvested 3 days later in cryoprotectant solution containing reservoir solution supplemented with 30% glycerol and flash cooled in liquid nitrogen.

A single dataset was collected at 100°K on a single $G_{1\text{-}440}$ crystal to 2.1 Å resolution collected at MASSIF-1 beamline (ESRF Grenoble France) (Svensson et al., 2018).

Structure determination and refinement

All diffraction data were integrated and reduced using XDS program package (Kabsch, 2010). $G_{1\text{-}440}$ crystals belonged to P622 space group. The structure was determined by molecular replacement with MOLREP (Vagin and Teplyakov, 2010) using G_{th} in its pre-fusion conformation as a search model (PDB 5I2S). Initial maps were clear enough to assess the presence of the C-terminal part of $G_{1\text{-}440}$. The model was iteratively built using COOT (Emsley et al., 2010) and refined with PHENIX (Afonine et al., 2012). The details of the crystallographic analysis are presented in Table S2. Structure representations were made using PyMol (PyMOL Molecular Graphics System. DeLano Scientific LLC, San Carlos, CA, USA. https://pymol.org/2/). RMSDs were computed with superpose (CCP4 supported program) (Krissinel and Henrick, 2004).

QUANTIFICATION AND STATISTICAL ANALYSIS

All numerical data were calculated and plotted with mean ± SD resulting from at least 3 independent biological replicates. Results were analyzed by two-tailed Student's t test (when comparing two means) or one sample t test (when comparing a sample mean to a known value). The statistical significance of the differences is indicated in the legend of the figures.

Cell Reports, Volume *32*

Supplemental Information

Identification of a pH-Sensitive Switch in VSV-G and a Crystal Structure of the G Pre-fusion State Highlight the VSV-G Structural Transition Pathway

Frauke Beilstein, Abbas Abou Hamdan, Hélène Raux, Laura Belot, Malika Ouldali, Aurélie A. Albertini, and Yves Gaudin

Supplemental information

The identification of a pH-sensitive switch in VSV G and a new crystal structure of G pre-fusion state highlight VSV G structural transition pathway

Frauke Beilstein, Abbas Abou Hamdan, Hélène Raux, Laura Belot, Malika Ouldali, Aurélie A. Albertini and Yves Gaudin

Supplementary figure

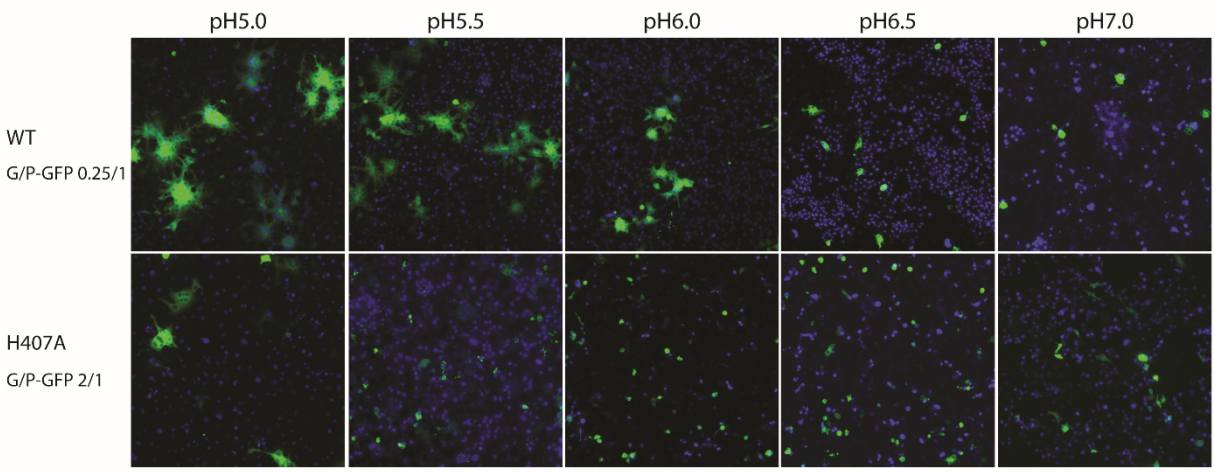

Figure S1. Related to Figure 3. Mutant H407A has a weak fusion activity at pH 5.

Fusion activity of WT G and mutant H407A was analyzed in a cell-cell fusion assay. BSR cells were transfected with plasmids expressing VSV G (either WT or mutant) and P-GFP, allowing easy observation of syncytia. In these experiments, cells were transfected either with a quarter of the amount of the plasmid expressing WT G used in figure 3 (Top line) or twice the amount of the plasmid expressing mutant H407A used in figure 3 (bottom line). At 24 h post-transfection, the cells were exposed for 10 min to DMEM adjusted to the indicated pH, which was then replaced by DMEM at pH 7.4. The cells were then kept at 37°C for 1 h before fixation. Nuclei were stained with DAPI.

Supplementary tables

His	Conserved across the vesiculovirus genus	Characteristics	Previously Mutated
8	No	Solvent exposed in both conformations.	Yes[1]
22	No	Change of environment during the conformational change.	No
33	No	Solvent exposed in both conformations.	No
60	Yes	Belongs to the pre-fusion histidine cluster.	No
80	Yes	Required for fusion. Involved in the formation of the interchain antiparallel beta sheet.	Yes[2]
132	Yes	Salt bridge with the neighbor protomer in the post-fusion trimer.	No
133	No	Solvent exposed in both conformations.	No
162	No	Belongs to the pre-fusion histidine cluster.	No
168	No	Solvent exposed in both conformations.	No
226	No	Solvent exposed in both conformations.	No
389	No	Facing D280 in the post-fusion conformation	No
397	No	Change of environment during the structural change	No
407	Yes	Belongs to the pre-fusion histidine cluster.	No
409	No	Belongs to the pre-fusion histidine cluster.	No

Table S1: List of histidine residues present in the ectodomain of VSV Indiana G, Related to Figure 1. Histidines in red correspond to those that have been mutated in this study. [1](Nikolic et al., 2018); [2](Baquero et al., 2017)

	VSV G 1-440
Wavelength	0.966
Resolution range	41.21 - 2.074 (2.148 - 2.074)
Space group	P 6 2 2
Unit cell	120.95 120.95 200.32 90 90 120
Total reflections	359583
Unique reflections	52870 (4971)
Multiplicity	6.8
Completeness (%)	99.50 (95.45)
Mean I/sigma(I)	8.27
Wilson B-factor	38.76
CC1/2	99.6 (39.6)
Reflections used in refinement	52861 (4971)
Reflections used for R-free	2600 (258)
R-work	0.2015 (0.2896)
R-free	0.2384 (0.3237)
Number of non-hydrogen atoms	3714
macromolecules	3406
ligands	97
solvent	211
Protein residues	432
RMS(bonds)	0.015
RMS(angles)	1.84
Ramachandran favored (%)	93.02
Ramachandran allowed (%)	6.51
Ramachandran outliers (%)	0.47
Rotamer outliers (%)	0.00
Clashscore	12.57
Average B-factor	61.87
macromolecules	61.05
ligands	108.11
solvent	53.85
Number of TLS groups	1

Statistics for the highest-resolution shell are shown in parentheses.

Table S2: Data collection and refinement statistics, Related to Figure 7.